

For publication in Radio Science, November 1994

---

## **Polarimetric scattering from layered media with multiple species of scatterers**

**S. V. Nghiem, R. Kwok, and S. H. Yueh**  
Jet Propulsion Laboratory  
California Institute of Technology  
Pasadena, California 91101

**J. A. Kong, C. C. Hsu, M. A. Tassoudji, and R. T. Shin**  
Department of Electrical Engineering and Computer Science  
and Research Laboratory of Electronics  
Massachusetts Institute of Technology  
Cambridge, Massachusetts 02139

---

**Mailing address : Dr. S. V. Nghiem, Jet Propulsion Laboratory  
Mail Stop 300-235, 4800 Oak Grove Drive, Pasadena, CA 91109**

# Polarimetric scattering from layered media with multiple species of scatterers

*S. V. Nghiem, R. Kwok, and S. H. Yueh*

*Jet Propulsion Laboratory, California Institute of Technology, Pasadena*

*J. A. Kong, C. C. Hsu, M. A. Tassoudji, and R. T. Shin*

*Department of Electrical Engineering and Computer Science*

*and Research Laboratory of Electronics*

*Massachusetts Institute of Technology, Cambridge*

Geophysical media are usually heterogeneous and contain multiple species of scatterers. In this paper, a model is presented to calculate effective permittivities and polarimetric backscattering coefficients of multi-species layered media. The same physical description is consistently used in the derivation of both permittivities and scattering coefficients. The strong permittivity fluctuation theory is extended to account for the multiple species of scatterers with a general ellipsoidal shape whose orientations are randomly distributed. Under the distorted Born approximation, polarimetric scattering coefficients are obtained. These calculations are applicable to the special cases of spheroidal and spherical scatterers. The model is used to study effects of scatterer shapes and multi-species mixtures on polarimetric signa-

tures of heterogeneous media. The multi-species model accounts for moisture content in media such as snowpack in an ice sheet. The results show a high sensitivity of backscattering coefficients to moisture. For frost-covered saline ice, model results for bare ice are compared with measured data at C band and then the frost-flower formation is simulated with a layer of fanlike ice crystals including brine infiltration over a rough interface. The results with the frost cover suggest a significant increase in scattering coefficients and a polarimetric signature closer to isotropic characteristics compared to the thin saline ice case.

## 1. INTRODUCTION

Natural geophysical media are usually inhomogeneous and contain various species of scatterers with different sizes, shapes, and permittivities. Much of the early work on multi-species media focused on calculations of effective permittivities. A multiphase dielectric mixture theory was presented by Tinga et al. [1979] with a summary of most important mixture relations derived by many authors. In a study of heterogeneous earth media such as brine-saturated rocks, it was found that the particle shape plays a major role in the effective electrical properties characterized by mixing formulas [Wait, 1989]. Expressions for effective permittivities of media with multiphase ellipsoids have been derived by Sihvola et al. [1988] whose results lead to generalized Lorentz-Lorenz, Polder-van Santen, and coherent potential-quasicrystalline approximation formulas with applications to snow and

sea ice.

The above formulations account for absorption loss in the inhomogeneous media. To include scattering effects, the strong permittivity fluctuation theory is used to calculate effective permittivities of multi-species media such as dry and wet snow and vegetation [Tsang and Kong, 1981a,b; Tsang et al., 1982]. For sea ice containing brine and air inclusions, effective permittivities are computed with the strong fluctuation theory at microwave frequencies [Stogryn, 1987]. For multi-species media with densely distributed particles, effective propagation constants are obtained for spherical scatterers under quasicrystalline and quasicrystalline with coherent potential approximations [Ding and Tsang, 1989].

Effective permittivities describe wave propagation and attenuation in inhomogeneous media. However, to interpret physical characteristics of the media from remote sensing radar data, electromagnetic scattering from multiple species of scatterers needs to be derived. Conventional backscattering coefficients are calculated with a model of sea ice containing spherical scatterers in isotropic media with rough surfaces [Tjuatja et al., 1992]. Polarimetric signatures of sea ice are derived with a model for ellipsoidal inclusions embedded in anisotropic layered media with rough interfaces [Nghiem et al., 1993]. These models consider a single species of scatterers (two-phase mixture) and are applicable when the inhomogeneities are dominantly consisted of scatterers of the same types. It is shown with a theoretical model of forest backscatter [Lang et al., 1993] that different species with different permittivities and structures can cause large variations in backscattering coefficients of pine trees for vertical polarization at C band. Polarimetric signatures of a layer of multi-species spheroidal scatterers are also studied based on vector radiative transfer theory [Tsang et al., 1990].

In this paper, both effective permittivities and polarimetric signatures are derived from the same physical description of inhomogeneous layered media. The difference with the above referenced papers is that this present work presents a consistent model for wave propagation, attenuation, and polarimetric scattering under the framework of the analytic wave theory, which simultaneously considers multiple species, ellipsoidal shape, large permittivity differences, absorption and scattering losses, preservation of phase information, multiple interactions with layer boundaries, and polarimetric signatures of the heterogeneous media. Effective permittivities are derived with random orientations of the multi-species non-spherical scatterers. The distorted Born approximation is applied to calculate polarimetric scattering coefficients in the covariance matrix [Nghiem *et al.*, 1990]. These calculations involve numerical integrations over Eulerian angles; however, analytical expressions are also obtained under the low-frequency approximation. Polarimetric signatures of media with multi-species mixing and various scatterer shapes are presented in examples for vegetation, snow, ice sheet, and sea ice.

## 2. EFFECTIVE PERMITTIVITY

The effective permittivity of a heterogeneous medium is composed of a quasi-static part and a scattering-effect part corresponding to the first and second terms, respectively, in the following expression [Tsang and Kong, 1981a]

$$\bar{\bar{\epsilon}}_{eff} = \bar{\bar{\epsilon}}_g + \epsilon_0 \left[ \bar{\bar{I}} - \bar{\bar{\xi}}_{eff} \cdot \langle \bar{\bar{S}} \rangle \right]^{-1} \cdot \bar{\bar{\xi}}_{eff} \quad (1)$$

where  $\bar{\bar{I}}$  is the unit dyad,  $\epsilon_0$  is the permittivity of free space,  $\bar{\bar{\epsilon}}_g$  is an auxiliary permittivity, and  $\bar{\bar{S}}$  is a dyadic coefficient. For a medium containing  $N$  species, effective dyadic scatterer

$\bar{\bar{\xi}}_{eff}$  is given by

$$[\bar{\bar{\xi}}_{eff}]_{jm} = \sum_{i=1}^N \int_0^{2\pi} d\gamma \int_0^\pi d\beta \int_0^{2\pi} d\alpha p(\alpha, \beta, \gamma) \sum_{k,l}^{x,y,z} \Gamma_{i\xi jklm}^{(0)} \left\{ k_0^2 \int_{-\infty}^{\infty} d\bar{k}' [\bar{G}_g(\bar{k}')]_{kl} \Phi_{i\xi}(\bar{k}') + [\bar{S}_i]_{kl} \right\} \Big|_{\alpha, \beta, \gamma} \quad (2)$$

under the condition  $||[\bar{\bar{\xi}}_{eff}]||_{jm} \ll 1$ . In (2), subscript  $i$  stands for species  $i$ ,  $k_0$  is the wave number in free space,  $\Gamma_{i\xi jklm}^{(0)}$  is the variance, and  $p(\alpha, \beta, \gamma)$  is the probability density function of orientations given by Eulerian angles  $\alpha$ ,  $\beta$ , and  $\gamma$ . In this paper, the random orientation distribution of the multi-species scatterers is considered. This requires the isotropic form of the Green's function  $\bar{G}_g$  [Nghiem *et al.*, 1990] and the auxiliary permittivity tensor becomes  $\bar{\bar{\epsilon}}_g = \epsilon_g \bar{I}$ .

The size and shape of scatterer species  $i$  are described with the Fourier transform  $\Phi_{i\xi}(\bar{k}')$  of the normalized local correlation function. For ellipsoids,  $\Phi_{i\xi}(\bar{k}')$  takes on the form

$$\Phi_{i\xi}(\bar{k}') = \frac{l_{ix'} l_{iy'} l_{iz'}}{\pi^2 (1 + k_x'^2 \ell_{ix'}^2 + k_y'^2 \ell_{iy'}^2 + k_z'^2 \ell_{iz'}^2)^2} \quad (3)$$

in which  $l_{ix'}$ ,  $l_{iy'}$ , and  $l_{iz'}$  are three different correlation lengths in the local coordinates corresponding to the minor, the meridian, and the major axes of an ellipsoidal scatterer of species  $i$ . The local principal coordinate system  $(x', y', z')$  of an ellipsoid is related to the global coordinate system  $(x, y, z)$  by Eulerian angles  $\alpha$ ,  $\beta$ , and  $\gamma$  as shown in appendix A.

To facilitate the derivation, the following principal variances are defined in the local coordinates as

$$\delta_{i\xi j'k'} = \delta_{i\xi k'j'} = f_{si} f_b (\xi_{ij'} - \xi_{bj'}) (\xi_{ik'} - \xi_{bk'}) \quad (4)$$

where  $j', k' = x', y', z'$ , subscript  $si$  denotes scatterer (indicated by  $s$ ) species  $i$ , subscript

$b$  is for the background medium, and the following definitions have been used

$$\xi_{ix'} = \frac{\epsilon_{si} - \epsilon_g}{\epsilon_0 + S_{ix'}(\epsilon_{si} - \epsilon_g)} \quad (5a)$$

$$\xi_{iy'} = \frac{\epsilon_{si} - \epsilon_g}{\epsilon_0 + S_{iy'}(\epsilon_{si} - \epsilon_g)} \quad (5b)$$

$$\xi_{iz'} = \frac{\epsilon_{si} - \epsilon_g}{\epsilon_0 + S_{iz'}(\epsilon_{si} - \epsilon_g)} \quad (5c)$$

For the background, (5) is used with subscript  $i$  replaced by  $b$  and species permittivity  $\epsilon_{si}$  by background permittivity  $\epsilon_b$ . In the global coordinates, the Eulerian transformation rotates the principal variances  $\delta_{ij'k'}$  to

$$\begin{aligned} \Gamma_{i\xi jklm}^{(0)} &= \delta_{ix'x'} a_{xjk} a_{xlm} + \delta_{ix'y'} a_{xjk} a_{ylm} + \delta_{ix'z'} a_{xjk} a_{zlm} \\ &+ \delta_{iy'y'} a_{yjk} a_{xlm} + \delta_{iy'z'} a_{yjk} a_{ylm} + \delta_{iy'z'} a_{yjk} a_{zlm} \\ &+ \delta_{iz'z'} a_{zjk} a_{xlm} + \delta_{iz'y'} a_{zjk} a_{ylm} + \delta_{iz'z'} a_{zjk} a_{zlm} \end{aligned} \quad (6)$$

where  $a_{jkl}$ 's have been defined in appendix B.

The condition of secular elimination is used to derive  $\epsilon_g$  and  $\bar{S}$  [Tsang *et al.*, 1981a; Yueh *et al.*, 1990; Nghiem *et al.*, 1993a,b]. This condition imposes  $\langle \bar{\xi}(\bar{r}) \rangle = 0$  where the ensemble average is obtained by

$$\langle \bar{\xi}(\bar{r}) \rangle = \int_0^{2\pi} d\gamma \int_0^\pi d\beta \int_0^{2\pi} d\alpha p(\alpha, \beta, \gamma) \bar{T}^{-1} \cdot \left[ f_b \bar{\xi}_b + \sum_{i=1}^N f_{si} \bar{\xi}_i \right] \cdot \bar{T} \quad (7)$$

In (7), the probability density function of orientations for randomly oriented scatterers is

$$p(\alpha, \beta, \gamma) = \sin \beta / (8\pi^2) \quad (8)$$

which renders  $\bar{\epsilon}_g$  isotropic. As shown in appendix B, this orientation distribution together with the secular elimination condition cast (7) into

$$f_b (\xi_{bx'} + \xi_{by'} + \xi_{bz'}) + \sum_{i=1}^N f_{si} (\xi_{ix'} + \xi_{iy'} + \xi_{iz'}) = 0 \quad (9)$$

where  $\xi$ 's have been defined by (5). Elements of  $\overline{\overline{S}}_i$  are calculated with the removal of the frequency independent parts in the effective scatterer terms as required by the secular elimination condition. Applying the symmetry of the ellipsoidal function leads to the following results

$$S_{iz'}(l_{ix'}, l_{iy'}, l_{iz'}) = \int_0^{2\pi} d\phi \frac{\epsilon_0(1+a_i)}{2\pi\epsilon_g a_i \sqrt{a_i}} [\sqrt{a_i} - \tan^{-1} \sqrt{a_i}] \quad (10a)$$

$$S_{iy'}(l_{ix'}, l_{iy'}, l_{iz'}) = S_{iz'}(l_{ix'}, l_{iz'}, l_{iy'}) \quad (10b)$$

$$S_{ix'}(l_{ix'}, l_{iy'}, l_{iz'}) = S_{iz'}(l_{iz'}, l_{iy'}, l_{ix'}) \quad (10c)$$

where principal branch cuts and principal Riemann sheets have been chosen for the square root and the inverse tangent functions. In (10), the integrations over  $\phi$  can be carried out numerically and  $a_i$  and  $\gamma_i$  are defined as

$$a_i = \gamma_i^2 - 1 \quad (11a)$$

$$\gamma_i = \left( \frac{\cos^2 \phi}{\gamma_{ix'}^2} + \frac{\sin^2 \phi}{\gamma_{iy'}^2} \right)^{-\frac{1}{2}} \quad (11b)$$

$$\gamma_{ix'} = \frac{l_{ix'}}{l_{iz'}}, \quad \gamma_{iy'} = \frac{l_{iy'}}{l_{iz'}} \quad (11c)$$

Then, the average dyadic coefficient  $\langle \overline{\overline{S}} \rangle$  in (1) is determined by

$$\begin{aligned} \langle \overline{\overline{S}} \rangle &= \sum_{i=1}^{N,b} f_{si} \int_0^{2\pi} d\gamma \int_0^\pi d\beta \int_0^{2\pi} d\alpha p(\alpha, \beta, \gamma) \overline{\overline{T}}^{-1} \cdot \begin{bmatrix} S_{ix'} & 0 & 0 \\ 0 & S_{iy'} & 0 \\ 0 & 0 & S_{iz'} \end{bmatrix} \cdot \overline{\overline{T}} \\ &= \frac{f_b}{3} (S_{bx'} + S_{bz'} + S_{bz'}) \overline{\overline{T}} + \sum_{i=1}^N \frac{f_{si}}{3} (S_{ix'} + S_{iz'} + S_{iz'}) \overline{\overline{T}} = \overline{\overline{S}} \end{aligned} \quad (12)$$

where  $\overline{\overline{S}}_b = \sum f_{si} \overline{\overline{S}}_i / \sum f_{si}$ . Equations (9) and (12) are used to solve for  $\epsilon_g$  and  $S$ 's with an iteration method.

To complete the calculation of the effective permittivity, let the quantity in the brackets in (2) be

$$\eta_{ijm}(\hat{r}') = k_0^2 \int_{-\infty}^{\infty} d\bar{k}' [\bar{G}_g(\bar{k}')]_{kl} \Phi_{i\xi}(\bar{k}') + [\bar{S}_i]_{kl} \quad (13)$$

In the local coordinates,  $\bar{\eta}_i(\hat{r}')$  is a diagonal tensor whose elements are

$$\eta_{ij'j'} = \eta_{ij'} = I_{ij'} + S_{ij'}, \quad j' = x', y', z' \quad (14)$$

where  $I_{ij'}$  involves the integration of dyadic Green's function and correlation function. The result for  $I_{iz'}$  is

$$I_{iz'} = \int_0^{2\pi} d\phi \frac{-\epsilon_0}{\pi \epsilon_g} (\mathcal{I}_{i\phi}^s + \mathcal{I}_{i\phi}^d) \quad (15a)$$

$$\mathcal{I}_{i\phi}^s = -\frac{\gamma_i^3}{2a_i^2} \left[ \frac{\sqrt{-\zeta}}{\vartheta_e} + \frac{\vartheta_e + \zeta}{\vartheta_e \sqrt{\vartheta_e}} \left( \frac{\pi}{2} - \tan^{-1} \frac{\sqrt{-\zeta}}{\sqrt{\vartheta_e}} \right) \right] \quad (15b)$$

$$\mathcal{I}_{i\phi}^d = \frac{\gamma_i^2}{2a_i^2} \left[ \frac{1 + a_i \nu_{gz'}^2}{\vartheta_o} + \frac{\vartheta_o(a_i + 2) - (b + a_i \nu_{gz'}^2)}{\vartheta_o \sqrt{\vartheta_o}} \left( \frac{\pi}{2} - \tan^{-1} \frac{1}{\sqrt{\vartheta_o}} \right) \right] \quad (15c)$$

$$\nu_{gz'}^2 = k_g^2 \ell_{iz'}^2, \quad k_g^2 = \omega^2 \mu_0 \epsilon_g, \quad \zeta = \gamma_i^2 \nu_{gz'}^2 \quad (15d)$$

$$b = \frac{\gamma_i^2 + \zeta}{a_i}, \quad \vartheta_o = b - 1, \quad \vartheta_e = b + \zeta \quad (15e)$$

The symmetry of the ellipsoid is used again to find  $I_{ix'}$  and  $I_{iy'}$  which are simply

$$I_{ix'}(\ell_{ix'}, \ell_{iy'}, \ell_{iz'}) = I_{iz'}(\ell_{iz'}, \ell_{iy'}, \ell_{ix'}) \quad (16)$$

$$I_{iy'}(\ell_{ix'}, \ell_{iy'}, \ell_{iz'}) = I_{iz'}(\ell_{ix'}, \ell_{iz'}, \ell_{iy'}) \quad (17)$$

To rotate  $\bar{\eta}_i(\hat{r}')$  into the global coordinates, the Eulerian transformation is applied.

Elements of  $\bar{\eta}_i(\hat{r})$  in the global coordinates are

$$\eta_{ikl} = \eta_{ix'} a_{xkl} + \eta_{iy'} a_{ykl} + \eta_{iz'} a_{zkl} = \eta_{ilk} \quad (18)$$

Variance  $\Gamma$  in (6) and quantity  $\eta$  in (18) are combined to define

$$\begin{aligned} \xi_{ijm}^{(0)} &= \sum_{k,l}^{x,y,z} \Gamma_{i\xi jklm}^{(0)} \eta_{ikl} = \sum_{u,v,w}^{x,y,z} \delta_{i\xi u'v'} \eta_{iw'} \\ &\quad (a_{uxj} a_{vxm} a_{wx} + a_{uxj} a_{vym} a_{wy} + a_{uxj} a_{vzm} a_{wx} \\ &\quad + a_{uyj} a_{vxm} a_{wyx} + a_{uyj} a_{vym} a_{wy} + a_{uyj} a_{vzm} a_{wyz} \\ &\quad + a_{uzj} a_{vxm} a_{wzx} + a_{uzj} a_{vym} a_{wzy} + a_{uzj} a_{vzm} a_{wzz}) \end{aligned} \quad (19)$$

After the integration over the Eulerian angles for the terms in (19), the effective scatterer tensor for species  $i$  becomes

$$\begin{aligned} \bar{\bar{\xi}}_{i\text{eff}} &= \int_0^{2\pi} d\gamma \int_0^\pi d\beta \int_0^{2\pi} d\alpha p(\alpha, \beta, \gamma) \bar{\bar{\xi}}_i^{(0)} \\ &= \frac{1}{3} (\delta_{i\xi x'x'} \eta_{ix'} + \delta_{i\xi y'y'} \eta_{iy'} + \delta_{i\xi z'z'} \eta_{iz'}) \bar{\bar{I}} \end{aligned} \quad (20)$$

Another method to find (20) is to carry out all tensor operations involving  $\Gamma$ 's and  $\eta$ 's in the local coordinates and then rotate the result into the global coordinates where appendix B is readily applicable to arrive at (20). Substituting (20) in (2) and using the result in (1) yield the effective permittivity

$$\bar{\bar{\epsilon}}_{\text{eff}} = \left[ \epsilon_g + \frac{\epsilon_o}{3} \sum_{i=1}^N (\delta_{i\xi x'x'} \eta_{ix'} + \delta_{i\xi y'y'} \eta_{iy'} + \delta_{i\xi z'z'} \eta_{iz'}) \right] \bar{\bar{I}} \quad (21)$$

The effective permittivity, as indicated in (21), is isotropic due to the random orientation of the scatterer species. The above result for the effective permittivity of an inhomogeneous medium containing multiple species of scatterers will reduce to that of a two-phase mixing medium containing a single species of randomly oriented spheroids embedded in a background medium [Yueh *et al.* 1990; Nghiem *et al.*, 1993a]. In the next section, the effective permittivity is used in the derivation of a complete set of polarimetric backscattering coefficients under the distorted Born approximation.

### 3. SCATTERING COEFFICIENTS

For applications to polarimetric remote sensing of geophysical media, it is necessary to derive the full set of polarimetric backscattering coefficients constituting the polarimetric covariance matrix. An electromagnetic wave incident on heterogeneous media is scattered by embedded inhomogeneities which also dictates the wave propagation and attenuation characterized by the effective permittivity obtained in the last section. Thus, the same physical description of the media used to calculate the effective permittivity must be used for a consistent derivation of the scattering coefficients.

Consider an electromagnetic wave impinging upon layered inhomogeneous media in the direction of wave vector  $\bar{k}_{0i}$  with an incident angle of  $\theta_{0i}$  as shown in figure 1. The upper half space is air and the underlying medium is homogenous. Each region in the layered configuration is inhomogeneous and contains multiple species of scatterers which are ellipsoidal and randomly oriented. Polarimetric scattering coefficients of the layered media are defined with ensemble averages of scattered fields with all polarization combinations. These averages are calculated with spatial integrations over products of dyadic Green's function  $G$  (DGFs), mean field  $F$ , and correlation function  $C$  as follows

$$\begin{aligned} \langle \bar{E}_{0s}(\bar{r}) \cdot \bar{E}_{0s}^*(\bar{r}) \rangle &= \sum_{n=1}^2 \sum_{t=1}^{N_n} \sum_{i,j,k,l,m}^{x,y,z} k_0^4 \int_0^{2\pi} d\gamma \int_0^\pi d\beta \int_0^{2\pi} d\alpha \\ &\cdot \int_{V_n} d\bar{r}_n \int_{V_n} d\bar{r}_n^o p_n(\alpha, \beta, \gamma) C_{t\xi n j k l m}(\bar{r}_n, \bar{r}_n^o; \alpha, \beta, \gamma) \\ &\cdot [\langle G_{0n i j}(\bar{r}, \bar{r}_n) \rangle \langle F_{n k}(\bar{r}_n) \rangle] \cdot [\langle G_{0n i l}(\bar{r}, \bar{r}_n^o) \rangle \langle F_{n m}(\bar{r}_n^o) \rangle]^* \quad (22) \end{aligned}$$

where  $t$  stands for the scatterer species  $t$  and  $N_n$  is the number of species in region  $n = 1, 2$ .

The DGFs and the mean fields are given by Nghiem et al. [1990].

Physical properties of the scatterers are characterized by correlation function  $C$  defined in the spatial and spectral domains as

$$C_{t\xi njklm}(\bar{r}_n, \bar{r}_n^o; \alpha, \beta, \gamma) = \langle \xi_{tnjk}(\bar{r}_n) \xi_{tnlm}^*(\bar{r}_n^o) | \alpha(\bar{r}_n), \beta(\bar{r}_n), \gamma(\bar{r}_n) \rangle \quad (23a)$$

$$= \int_{-\infty}^{\infty} d\bar{\beta} \Phi_{tnjklm}(\bar{\beta}) e^{-i\bar{\beta} \cdot (\bar{r}_n - \bar{r}_n^o)}, \quad n = 1, 2 \quad (23b)$$

which is expressed in the global coordinate system  $(\hat{x}, \hat{y}, \hat{z})$  and related by the rotation transformation with Eulerian angles  $(\alpha, \beta, \gamma)$  to those in the local coordinate system  $(\hat{x}', \hat{y}', \hat{z}')$ . Function  $\Phi_{tnjklm}$  is a product of variance  $\Gamma_{tnjklm}$  and normalized functional part  $\Phi_{t\xi n}$

$$\Phi_{tnjklm}(\bar{\beta}) = \Gamma_{tnjklm} \Phi_{t\xi n}(\bar{\beta}) \quad (24)$$

where  $\Phi_{t\xi n}$  is defined in the same manner as in (3) for ellipsoidal scatterers with  $l_{ix'}$ ,  $l_{iy'}$ , and  $l_{iz'}$  replaced by  $l_{tnx'}$ ,  $l_{tny'}$ , and  $l_{tnz'}$  for species  $t$  in region  $n$ .

Variance  $\Gamma_{tnjklm}$  is related to local principal variance  $\delta_{tnj'k'}$  which is defined as in (4) but the last term in the product is complex conjugated

$$\delta_{tnj'k'} = \delta_{tnk'j'}^* = f_{stn} f_{bn} (\xi_{tnj'} - \xi_{bnj'}) (\xi_{tnk'} - \xi_{bnk'})^* \quad (25)$$

Note that all quantities in the right-hand side of (25) is the same as in the calculation of the effective permittivity; here subscript  $t$  (instead of  $i$  as in (4)) is used to denote the species and subscript  $n$  is for region  $n$  as indicated earlier. For  $\xi$ 's in (25), (5) is used with subscript  $i$  replaced by  $tn$ ,  $\epsilon_{tn}$  for the scatterers,  $\epsilon_{bn}$  for the background, and  $\epsilon_{gn}$  for the auxiliary permittivity in region  $n$ . After the Eulerian transformations into the global coordinates, element  $\Gamma_{tnjklm}$  in the fourth-rank variance tensor  $\bar{\bar{\Gamma}}_{tn}$  becomes

$$\Gamma_{tnjklm} = \sum_{u,v}^{x,y,z} \delta_{tnuv} a_{ujk} a_{vlm}$$

$$\begin{aligned}
&= \delta_{tnx'x'} a_{xjk} a_{xlm} + \delta_{tnx'y'} a_{xjk} a_{ylm} + \delta_{tnx'z'} a_{xjk} a_{zlm} \\
&+ \delta_{tny'x'} a_{yjk} a_{xlm} + \delta_{tny'y'} a_{yjk} a_{ylm} + \delta_{tny'z'} a_{yjk} a_{zlm} \\
&+ \delta_{tnz'x'} a_{zjk} a_{xlm} + \delta_{tnz'y'} a_{zjk} a_{ylm} + \delta_{tnz'z'} a_{zjk} a_{zlm}
\end{aligned} \tag{26}$$

When integrations over Eulerian angles of the probability density function (8) for random orientations are applied to the variances in (26), the averaged variance is defined, for latter consideration, as

$$\Delta_{tnjklm} = \sum_{u,v}^{x,y,z} \int_0^{2\pi} d\gamma \int_0^\pi d\beta \int_0^{2\pi} d\alpha p_n(\alpha, \beta, \gamma) \delta_{tnuv} a_{ujk} a_{vlm} \tag{27}$$

Each of the 6 subscripts  $u, j, k, v, l,$  or  $m$  has three components  $x, y,$  and  $z$ ; thus, there are  $3^6$  or 729 terms to be integrated over the Eulerian angles in (27) and among those 540 integrations turn out to be zero. The non-zero results are presented in appendix C.

With the above correlation functions, correlations of the scattered fields can now be determined by (22) to obtain polarimetric scattering coefficients defined by [Nghiem *et al.*, 1990]

$$\sigma_{\mu\tau\nu\kappa} = \lim_{\substack{r \rightarrow \infty \\ A \rightarrow \infty}} \frac{4\pi r^2}{A} \frac{\langle E_{\mu s} E_{\nu s}^* \rangle}{E_{\tau o} E_{\kappa o}^*} \tag{28}$$

where subscript  $o$  denotes incident fields and  $s$  for scattered fields, subscripts  $\mu, \nu, \tau,$  or  $\kappa$  can be horizontal ( $h$ ) or vertical ( $v$ ) polarization,  $r$  is the range from the antenna to the target, and  $A$  is the illuminated area. Conventional backscattering coefficients are  $\sigma_{hh} \equiv \sigma_{hhhh}, \sigma_{vv} \equiv \sigma_{vvvv},$  and  $\sigma_{hv} \equiv \sigma_{hvhv}.$  Correlation coefficient  $\rho$  between the horizontal and vertical returns is  $\rho = \sigma_{hhvv} / \sqrt{\sigma_{hhhh} \sigma_{vvvv}}.$

All integrations in (22) are carried out analytically except the triple integration over the Eulerian angles which may be intensive in computer time for numerical solution. Under

the low-frequency approximation, an analytical solution, which is computationally efficient, is obtained and the result is expressed as

$$\begin{aligned} \sigma_{\mu\tau\nu\kappa} = & \pi k_0^4 \sum_{t=1}^{N_1} \sum_{a,b,c,d,j,k,l,m}^{-1,1} \sum_{x,y,z} \Psi_{1\mu\tau,jk}^{ab} \Psi_{1\nu\kappa,lm}^{cd*} W_{t1jklm}^{abcd} \\ & + \pi k_0^4 \sum_{t=1}^{N_2} \sum_{p,q,r,s}^{d,u} \sum_{j,k,l,m} \Psi_{2\mu\tau,jk}^{pq} \Psi_{2\nu\kappa,lm}^{rs*} W_{t2jklm}^{pqrs} \end{aligned} \quad (29)$$

in which  $-1$  or  $d$  is for down-going wave and  $1$  or  $u$  for up-going wave. Expressions for  $\Psi$ 's have been derived by Nghiem et al. [1990]. Quantity  $W_{t1jklm}^{abcd}$  for region 1 in (29) is

$$W_{t1jklm}^{abcd} = \int_0^{2\pi} d\gamma \int_0^\pi d\beta \int_0^{2\pi} d\alpha p(\alpha, \beta, \gamma) \Gamma_{t1jklm} I_{t1}^{abcd} \quad (30)$$

where  $I_{t1}^{abcd}$  is the integral of the correlation function and the phase in region 1 over the  $z$  component of the spectral domain and thickness  $d_1$ ; the integral is carried out under the low frequency condition as

$$\begin{aligned} I_{t1}^{abcd} &= \int_{-\infty}^{\infty} d\beta_z \Phi_{t1\xi}(2\bar{k}_{\rho i}, \beta_z) \int_{-d_1}^0 dz_1 e^{-i(\beta_z - \kappa_{ab})z_1} \int_{-d_1}^0 dz_1^o e^{i(\beta_z - \kappa_{cd})z_1^o} \\ &\approx 2\pi i \Phi_{t1\xi}(0) \left[ \frac{e^{-i(\kappa_{ab} - \kappa_{cd})d_1} - 1}{\kappa_{ab} - \kappa_{cd}} \right] \end{aligned} \quad (31)$$

With (26), (27), and (30)  $W_{t1jklm}^{abcd}$  is arranged in the following simple form

$$W_{t1jklm}^{abcd} = \Delta_{t1jklm} I_{t1}^{abcd} \quad (32)$$

Similarly, quantity  $W_{t2jklm}^{pqrs}$  for region 2 in (29) is

$$W_{t2jklm}^{pqrs} = \int_0^{2\pi} d\gamma \int_0^\pi d\beta \int_0^{2\pi} d\alpha p(\alpha, \beta, \gamma) \Gamma_{t2jklm} I_{t2}^{pqrs} \quad (33)$$

where the integral of  $I_{t2}^{pqrs}$  is carried out under the low frequency approximation for thickness  $(d_2 - d_1)$  of region 2 as

$$\begin{aligned} I_{t2}^{pqrs} &= \int_{-\infty}^{\infty} d\beta_z \Phi_{t2\xi}(2\bar{k}_{\rho i}, \beta_z) \int_{-d_2}^{-d_1} dz_2 e^{-i(\beta_z - \kappa_{pq})z_2} \int_{-d_2}^{-d_1} dz_2^o e^{i(\beta_z - \kappa_{rs})z_2^o} \\ &= 2\pi i \Phi_{t2\xi}(0) \left[ \frac{e^{-i(\kappa_{pq} - \kappa_{rs})d_2} - e^{-i(\kappa_{pq} - \kappa_{rs})d_1}}{\kappa_{pq} - \kappa_{rs}} \right] \end{aligned} \quad (34)$$

From the results in (26), (27), and (33), it is observed that  $W_{t_2jklm}^{pqrs}$  is simply

$$W_{t_2jklm}^{pqrs} = \Delta_{t_2jklm} I_{t_2}^{pqrs} \quad (35)$$

Note that the above results for the polarimetric scattering coefficients are expressed in the scattered basis. Both scattering regions in this configuration contain multiple species of ellipsoidal and the scattering media are effectively isotropic due to the random orientation. For a simpler configuration such as a half space or a scattering layer over a half space, the results are applicable by just setting the appropriate thicknesses. In the next section, the model is applied to study the polarimetric scattering properties from heterogeneous media.

## 4. RESULTS

### 4.1. Effects of Scatterer Shapes

In natural media, the shape of scatterers such as ice grains in snow is particularly subjected to temperature, medium metamorphoses, or environmental variations. The model in this paper accounts for various shapes which can be spherical, prolate or oblate spheroidal, or ellipsoidal in general. For an inhomogeneous medium with a fixed number of scatterers and fractional volume, the shape of the scatterers is a significant factor on the effective permittivity and the scattering coefficients of the medium. To study effects of the scatterer shape, consider a layered medium described in figure 2. The scattering region consists of an air background and embedded scatterers of 20% fractional volume and permittivity  $(3.15 + i0.002)\epsilon_0$  for ice at the C-band frequency of  $f = 5$  GHz. The underlying medium has a permittivity of  $(6.0 + i0.6)\epsilon_0$  which is in the permittivity range for soil.

Four different shapes of scatterers are investigated: spherical, prolate spheroidal, oblate spheroidal, and ellipsoidal. The fractional volume and the number of scatterers are kept the same in all cases and the non-spherical scatterers are randomly oriented. For the ellipsoidal shape, the longest correlation length is taken to be equal to that of the prolate spheroidal shape, the shortest correlation length is the same as that of the oblate spheroid, and the meridian correlation is chosen by setting the surface area (defined by the two longer correlation lengths) identical to that of the oblate spheroid. Correlation lengths and calculated effective permittivities corresponding to the various shapes are reported in table 1. It is seen that the effective permittivity is increasing when the scatterer shape varies from spherical, to prolate spheroidal, and then to oblate spheroidal forms. Permittivity results for the ellipsoids and oblate spheroids are similar due to the similar cross sections of the scatterers in the two cases.

Shape	$l_{1x'}$	$l_{1y'}$	$l_{1z'}$	$\epsilon_{eff1}$
Spherical	0.15 mm	0.15 mm	0.15 mm	$(1.29 + i 1.95 \times 10^{-4}) \epsilon_0$
Prolate	0.05 mm	0.05 mm	1.35 mm	$(1.31 + i 2.27 \times 10^{-4}) \epsilon_0$
Oblate	0.58 mm	0.58 mm	0.01 mm	$(1.33 + i 2.63 \times 10^{-4}) \epsilon_0$
Ellipsoidal	1.35 mm	0.25 mm	0.01 mm	$(1.32 + i 2.64 \times 10^{-4}) \epsilon_0$

Table 1. Correlation lengths and effective permittivities.

Differences in the scatterer shape are also manifested in scattering coefficients. Copolarized backscattering coefficients for different scatterer shapes are shown in figure 3. Oscillations in the curves of the scattering coefficients are due to multiple interactions with

the layer boundaries. The copolarized backscattering increases as the scatterer cross section increases from the spherical, to prolate, and then to oblate spheroidal form. The copolarization results for the ellipsoidal and the oblate spheroidal forms are similar. For cross-polarized returns, the spherical case gives zero value under the first-order distorted Born approximation. Cross-polarized backscattering coefficients for non-spherical scatterers are plotted as a function of incident angles in figure 4. The oblate spheroids provide the highest returns while the ellipsoids and the prolate spheroids have a similar cross-polarization effect due to the same size in their longest correlation lengths. As illustrated, the ellipsoids behave as a hybrid between the oblate and the prolate spheroids.

A common feature in all of the cases for the different shapes is the effective isotropy of the inhomogeneous medium. For the case of non-spherical scatterers, the medium is rendered isotropic by random scatterer orientations with no preferred direction. Wave speed and attenuation in the inhomogeneous isotropic medium is the same for horizontal and vertical waves. This results in correlation coefficient  $\rho$  between  $h$  and  $v$  waves with a small phase. Magnitudes of  $\rho$  plotted in figure 5 show a similar variation as a function of incident angles for the different shapes of the scatterers with a stronger decorrelation effect from non-spherical scatterers.

#### *4.2. Effects of Multiple Species*

The multi-species model in this paper allows the coexistence of disc-like and needle-like scatterers. Effects of multiple species are studied with the configuration described in figure 6, which corresponds to a soybean canopy [*Case 9-03-86, Nghiem et al., 1993a*] where the canopy was modeled with only disc-like scatterers. The soil surface is rough and

all input parameters are given by Nghiem et al. [1993a].

Now, needle-like scatterers are introduced into the canopy by allocating part of the total scatterer fractional volume to the new scatterer species whose permittivity is taken to be the same as that of the disc-like scatterers. The needle-like form is depicted by a prolate spheroidal shape with correlation lengths of 0.3 mm and 5.0 mm. Note that the volume of an individual needle-like scatterer is much smaller than that of the disc-like scatterer for the given parameters. Three cases are considered here: Case 1 has 100% oblate spheroids, Case 2 has 85% oblate and 15% prolate, and Case 3 has 70% oblate and 30% prolate spheroids.

Backscattering coefficients decrease, as seen in figure 7, for increasing needle-like species, which has a smaller total cross section. Figure 7 also shows that the decrease in the copolarized returns is more than that in the cross-polarized return. Again due to the effective isotropy, the phase of correlation coefficient  $\rho$  is small for the cases under consideration. While the magnitude of  $\rho$  for different mixtures are similar as indicated in figure 8, intensity ratio  $e = \sigma_{hv}/\sigma_{hh}$  is higher for a mixture containing more needle-like scatterers as shown in figure 9. This will result in a copolarized signature with a higher pedestal [Nghiem et al., 1990] indicating a stronger depolarization effect.

#### 4.3. Applications

This section presents applications of the multi-species model to study polarimetric scattering signatures from inhomogeneous media. A very lossy species of scatterers with a high permittivity strongly affects wave propagation, attenuation, and scattering in a multi-species medium. This model includes such a species together with other scattering

species to investigate effects of moisture in a scattering medium such as polar ice sheets. Effects of frost flowers on thin saline ice are also studied with a multi-species mixtures of fanlike ice crystals and brine inclusions.

Temperature changes cause variations in moisture content of snowpack such as polar ice sheets, which are important to global climate due to their vast coverage [Thomas *et al.*, 1985]. The configuration in figure 10 is a half space consisting of an air background and two species of spherical scatterers: one with fractional volume of 0.3 and a relative permittivity of  $3.15 + i0.0012$  for ice grain, the other with variable fractional volume and a relative permittivity of  $65 + i34$  for water. Correlation lengths are determined from scatterer sizes [Yueh *et al.*, 1990]. Backscattering coefficient  $\sigma_{vv}$  at 5.3 GHz and  $20^\circ$  incident angle, corresponding to the operating parameters of ERS-1 SAR (the First European Remote Sensing Synthetic Aperture Radar), is plotted as a function of ice grain size for various moisture contents from dry to wet conditions in figure 11. The results show that a small increase in moisture content (1%) can cause a decrease in the backscatter by several dB and the change in backscatter is larger for a drier condition.

Leads in the Arctic icepack are important to heat exchange with the atmosphere and salt flux into the upper ocean [Maykut, 1982]. Surface characteristics of thin sea ice in leads are dominated by the formation of frost flowers with a high salinity [Perovich and Richter-Menger, 1994]. This layer is simulated with a mixture containing randomly oriented ellipsoids and brine infiltration by a volume ratio of three parts ice and one part brine [Perovich and Richter-Menger, 1994]. The ice crystals are characterized with correlation lengths  $\ell_{11x'} = 0.1$  mm,  $\ell_{11y'} = 2$  mm, and  $\ell_{11z'} = 3$  mm to describe the fanlike form. Covered under the multi-species medium is an anisotropic layer of saline

ice composed of ellipsoidal brine inclusions preferentially oriented in the vertical direction in an ice background [Nghiem *et al.*, 1993b]. The inhomogeneities in the ice layer are dominated by brine inclusions and this layer is modeled with a single scattering species. Model characterization parameters are given in figure 12 for the layered media. Figure 13 compared polarimetric backscattering results obtained from the model with measured data obtained by the JPL polarimetric scatterometer at C-band (center frequency at 5 GHz) during the Cold Regions Research and Engineering Laboratory Experiment in 1993 (CRRELEX93) [Nghiem *et al.*, 1994] for thin saline ice. The continuous curves without symbol S compare well with the measured data. These curves are for the layered medium with a smooth surface without the covering layer, which correspond to the configuration of the bare saline ice for the CRRELEX93 measurements.

Then, the covering layer is included in the model to simulate the frost-flower formation. Note that the interface between this formation and the saline ice has some roughness described by an rms height of  $\sigma_s = 1$  mm and a surface correlation length of  $\ell_s = 1$  cm. This small-scale surface roughness characterizes bumps or small protrusions which are suggested by Perovich and Richter-Menger [1994] to serve as nucleation sites for the frost flowers. Polarimetric scattering from the surface roughness is calculated with the small perturbation method and included in the total polarimetric signatures [Nghiem *et al.*, 1993b]. The curves with symbol S on figure 13a indicate that this covering layer can increase copolarized backscattering coefficients by several dB while there is little impact on the cross-polarized return. Figures 13b and 13c show that the complex correlation coefficient  $\rho$  has a magnitude closer to one and a smaller phase; this behavior is more similar to the isotropic scattering characteristics. This is caused by the random orientation of

the ellipsoids in the covering layer and the nondirectional feature of the surface roughness. Figure 14 compares the normalized polarization signatures  $\sigma_n$  as a function of orientation angle  $\alpha_c$  and ellipticity angle  $\beta_c$  [Nghiem *et al.*, 1990]. The signature of the covered layered medium has a maximum in the middle ( $\alpha_c = 90^\circ$  and  $\beta_c = 0^\circ$ ) and a lower pedestal corresponding to a weaker depolarization effect [Nghiem *et al.*, 1990].

## 5. SUMMARY

This paper presents a model for layered inhomogeneous media containing multiple species of scatterers to calculate polarimetric backscattering signatures. The species are allowed to have different size, shape, and permittivity. The strong permittivity fluctuation theory is extended to account for the multi-species in the derivation of the effective permittivity with a random distribution of orientations characterized with Eulerian rotation angles.

Polarimetric backscattering coefficients are obtained consistently with the same physical description used in the effective permittivity calculation. Under the first-order distorted Born approximation, results for the scattering coefficients contain triple integrations over Eulerian angles, which can be carried out numerically. Analytical results are also obtained under the low-frequency approximation involving 729 terms for the random orientation distribution. The model indicates that non-spherical scatterers with larger cross section give higher effective permittivity and stronger scattering effects. The random orientation renders the medium isotropic for all scatterer shapes; however, the shapes of the scatterers are important to cross-polarized returns and magnitudes of polarimet-

ric correlation coefficient  $\rho$ . For a mixture of oblate (disc-like) and prolate (needle-like) spheroids, the oblate species contributes more to the total backscatter and the prolate species increases the cross-polarized intensity ratio  $e = \sigma_{hv}/\sigma_{hh}$ .

The multi-species model allows the inclusion of moisture in a scattering medium. The model indicates that backscattering coefficients for the vertical polarization at C band (ERS-1 polarization and frequency) are very sensitive to moisture content in snowpack. Effects of a multi-species covering layer such as frost-covered saline ice is also studied. Theoretical results for bare saline compare well with measured data at 5 GHz from CR-RELEX93. Then, the model is used to simulate the frost cover with a layer of fanlike crystals with brine infiltration. The results suggest that the frost cover with a rough interface can significantly increase the backscatter from thin saline ice and the polarimetric signature becomes closer to the isotropic characteristics. With the consideration of multiple species, the model advances toward a better representation of geophysical media. However, the media in natural conditions are more complicated and the model needs to be extended to account for multi-species in anisotropic media such as columnar sea ice with air and brine inclusions under environmental effects such as temperature variations.

## APPENDICES

### *A. Eulerian Rotations between Local and Global Coordinates*

To relate the local scatterer coordinate system  $(x', y', z')$  to the global coordinate system  $(x, y, z)$ , Eulerian angle  $\alpha$ ,  $\beta$ , and  $\gamma$  are used as illustrated in figure A1.

The rotation  $\alpha$  ( $0 < \alpha < 2\pi$ ) about  $z'$  axis,  $\beta$  ( $0 < \beta < \pi$ ) about  $y_1$  axis, and

$\gamma$  ( $0 < \gamma < 2\pi$ ) about  $z_2$  axis are described with the following relations

$$\begin{bmatrix} x_1 \\ y_1 \\ z_1 \end{bmatrix} = \overline{\overline{T}}_\alpha \cdot \begin{bmatrix} x' \\ y' \\ z' \end{bmatrix} = \begin{bmatrix} \cos \alpha & \sin \alpha & 0 \\ -\sin \alpha & \cos \alpha & 0 \\ 0 & 0 & 1 \end{bmatrix} \cdot \begin{bmatrix} x' \\ y' \\ z' \end{bmatrix} \quad (\text{A1a})$$

$$\begin{bmatrix} x_2 \\ y_2 \\ z_2 \end{bmatrix} = \overline{\overline{T}}_\beta \cdot \begin{bmatrix} x_1 \\ y_1 \\ z_1 \end{bmatrix} = \begin{bmatrix} \cos \beta & 0 & -\sin \beta \\ 0 & 1 & 0 \\ \sin \beta & 0 & \cos \beta \end{bmatrix} \cdot \begin{bmatrix} x_1 \\ y_1 \\ z_1 \end{bmatrix} \quad (\text{A1b})$$

$$\begin{bmatrix} x \\ y \\ z \end{bmatrix} = \overline{\overline{T}}_\gamma \cdot \begin{bmatrix} x_2 \\ y_2 \\ z_2 \end{bmatrix} = \begin{bmatrix} \cos \gamma & \sin \gamma & 0 \\ -\sin \gamma & \cos \gamma & 0 \\ 0 & 0 & 1 \end{bmatrix} \cdot \begin{bmatrix} x_2 \\ y_2 \\ z_2 \end{bmatrix} \quad (\text{A1c})$$

and the resultant Eulerian transformation which rotates the global to the local scatterer coordinates is

$$\begin{aligned} \begin{bmatrix} x' \\ y' \\ z' \end{bmatrix} &= \overline{\overline{T}} \cdot \begin{bmatrix} x \\ y \\ z \end{bmatrix} = \left[ \overline{\overline{T}}_\gamma \cdot \overline{\overline{T}}_\beta \cdot \overline{\overline{T}}_\alpha \right]^{-1} \cdot \begin{bmatrix} x \\ y \\ z \end{bmatrix} \\ &= \begin{bmatrix} \cos \gamma \cos \beta \cos \alpha - \sin \gamma \sin \alpha \\ \cos \gamma \cos \beta \sin \alpha + \sin \gamma \cos \alpha \\ -\cos \gamma \sin \beta \\ -\sin \gamma \cos \beta \cos \alpha - \cos \gamma \sin \alpha \\ -\sin \gamma \cos \beta \sin \alpha + \cos \gamma \cos \alpha \\ \sin \gamma \sin \beta \\ \sin \beta \cos \alpha \\ \sin \beta \sin \alpha \\ \cos \beta \end{bmatrix} \cdot \begin{bmatrix} x \\ y \\ z \end{bmatrix} \end{aligned} \quad (\text{A2})$$

### B. Average over Eulerian Angles

This appendix shows the average over the random orientation, described by Eulerian angles, of the product between tensor  $\bar{\xi}$  and orientation probability density function  $p(\alpha, \beta, \gamma)$ . The averaging integral is

$$\langle \bar{\xi}(\bar{r}) \rangle = \int_0^{2\pi} d\gamma \int_0^\pi d\beta \int_0^{2\pi} d\alpha p(\alpha, \beta, \gamma) \bar{T}^{-1} \cdot \bar{\xi}(\hat{r}') \cdot \bar{T} \quad (\text{B1})$$

where  $p(\alpha, \beta, \gamma) = \sin \beta / (8\pi^2)$  and rotation tensor  $\bar{T}$  is given by

$$\bar{T} = \begin{bmatrix} \cos \gamma \cos \beta \cos \alpha - \sin \gamma \sin \alpha & -\sin \gamma \cos \beta \cos \alpha - \cos \gamma \sin \alpha & \sin \beta \cos \alpha \\ \cos \gamma \cos \beta \sin \alpha + \sin \gamma \cos \alpha & -\sin \gamma \cos \beta \sin \alpha + \cos \gamma \cos \alpha & \sin \beta \sin \alpha \\ -\cos \gamma \sin \beta & \sin \gamma \sin \beta & \cos \beta \end{bmatrix} \quad (\text{B2})$$

Tensor  $\bar{\xi}(\hat{r})$  in the global coordinates  $(x, y, z)$  is obtained with the rotation operation

$$\bar{\xi}(\hat{r}) = \bar{T}^{-1} \cdot \bar{\xi}(\hat{r}') \cdot \bar{T} = \bar{T}^{-1} \cdot \begin{bmatrix} \xi_{x'} & 0 & 0 \\ 0 & \xi_{y'} & 0 \\ 0 & 0 & \xi_{z'} \end{bmatrix} \cdot \bar{T} = \begin{bmatrix} \xi_{xx} & \xi_{xy} & \xi_{xz} \\ \xi_{yx} & \xi_{yy} & \xi_{yz} \\ \xi_{zx} & \xi_{zy} & \xi_{zz} \end{bmatrix} \quad (\text{B3})$$

Explicitly, the elements of  $\bar{\xi}(\hat{r})$  in the global coordinates are

$$\begin{aligned} \xi_{xx} &= \xi_{x'} (\cos^2 \gamma \cos^2 \beta \cos^2 \alpha + \sin^2 \gamma \sin^2 \alpha - 2 \sin \gamma \cos \gamma \cos \beta \sin \alpha \cos \alpha) \\ &+ \xi_{y'} (\cos^2 \gamma \cos^2 \beta \sin^2 \alpha + \sin^2 \gamma \cos^2 \alpha + 2 \sin \gamma \cos \gamma \cos \beta \sin \alpha \cos \alpha) \\ &+ \xi_{z'} (\cos^2 \gamma \sin^2 \beta) = \xi_{x'} a_{xxx} + \xi_{y'} a_{yxx} + \xi_{z'} a_{zxx} \end{aligned} \quad (\text{B4a})$$

$$\begin{aligned} \xi_{xy} &= -\xi_{x'} (\sin \gamma \cos \gamma \cos^2 \beta \cos^2 \alpha + \cos^2 \gamma \cos \beta \sin \alpha \cos \alpha \\ &- \sin^2 \gamma \cos \beta \sin \alpha \cos \alpha - \sin \gamma \cos \gamma \sin^2 \alpha) \end{aligned}$$

$$\begin{aligned}
& -\xi_{y'} (\sin \gamma \cos \gamma \cos^2 \beta \sin^2 \alpha - \cos^2 \gamma \cos \beta \sin \alpha \cos \alpha \\
& + \sin^2 \gamma \cos \beta \sin \alpha \cos \alpha - \sin \gamma \cos \gamma \cos^2 \alpha) \\
& -\xi_{z'} (\sin \gamma \cos \gamma \sin^2 \beta) = \xi_{x'} a_{xxy} + \xi_{y'} a_{yxy} + \xi_{z'} a_{zxy}
\end{aligned} \tag{B4b}$$

$$\begin{aligned}
\xi_{xz} &= \xi_{x'} (\cos \gamma \sin \beta \cos \beta \cos^2 \alpha - \sin \gamma \sin \beta \sin \alpha \cos \alpha) \\
& + \xi_{y'} (\cos \gamma \sin \beta \cos \beta \sin^2 \alpha + \sin \gamma \sin \beta \sin \alpha \cos \alpha) \\
& + \xi_{z'} (-\cos \gamma \sin \beta \cos \beta) = \xi_{x'} a_{xxz} + \xi_{y'} a_{yxz} + \xi_{z'} a_{zzz}
\end{aligned} \tag{B4c}$$

$$\xi_{yx} = \xi_{x'} a_{xyx} + \xi_{y'} a_{yyx} + \xi_{z'} a_{zyx} = \xi_{x'} a_{xxy} + \xi_{y'} a_{yxy} + \xi_{z'} a_{zxy} \tag{B4d}$$

$$\begin{aligned}
\xi_{yy} &= \xi_{x'} (\sin^2 \gamma \cos^2 \beta \cos^2 \alpha + \cos^2 \gamma \sin^2 \alpha + 2 \sin \gamma \cos \gamma \cos \beta \sin \alpha \cos \alpha) \\
& + \xi_{y'} (\sin^2 \gamma \cos^2 \beta \sin^2 \alpha + \cos^2 \gamma \cos^2 \alpha - 2 \sin \gamma \cos \gamma \cos \beta \sin \alpha \cos \alpha) \\
& + \xi_{z'} (\sin^2 \gamma \sin^2 \beta) = \xi_{x'} a_{xyy} + \xi_{y'} a_{yyy} + \xi_{z'} a_{zyy}
\end{aligned} \tag{B4e}$$

$$\begin{aligned}
\xi_{yz} &= -\xi_{x'} (\sin \gamma \sin \beta \cos \beta \cos^2 \alpha + \cos \gamma \sin \beta \sin \alpha \cos \alpha) \\
& - \xi_{y'} (\sin \gamma \sin \beta \cos \beta \sin^2 \alpha - \cos \gamma \sin \beta \sin \alpha \cos \alpha) \\
& - \xi_{z'} (-\sin \gamma \sin \beta \cos \beta) = \xi_{x'} a_{xyz} + \xi_{y'} a_{yyz} + \xi_{z'} a_{zyz}
\end{aligned} \tag{B4f}$$

$$\xi_{zx} = \xi_{x'} a_{xzx} + \xi_{y'} a_{yzx} + \xi_{z'} a_{zzx} = \xi_{x'} a_{xxz} + \xi_{y'} a_{yxz} + \xi_{z'} a_{zzz} \tag{B4g}$$

$$\xi_{zy} = \xi_{x'} a_{xzy} + \xi_{y'} a_{yzy} + \xi_{z'} a_{zzy} = \xi_{x'} a_{xyx} + \xi_{y'} a_{yyx} + \xi_{z'} a_{zyx} \tag{B4h}$$

$$\begin{aligned}
\xi_{zz} &= \xi_{x'} (\sin^2 \beta \cos^2 \alpha) + \xi_{y'} (\sin^2 \beta \sin^2 \alpha) + \xi_{z'} \cos^2 \beta \\
& = \xi_{x'} a_{xzz} + \xi_{y'} a_{yzz} + \xi_{z'} a_{zzz}
\end{aligned} \tag{B4i}$$

Integrating over the above elements yields

$$\langle \xi_{xx} \rangle = \int_0^{2\pi} d\gamma \int_0^\pi d\beta \int_0^{2\pi} d\alpha p(\alpha, \beta, \gamma) \xi_{xx} = \frac{1}{3} (\xi_{x'} + \xi_{y'} + \xi_{z'}) \quad (\text{B5a})$$

$$\langle \xi_{yy} \rangle = \int_0^{2\pi} d\gamma \int_0^\pi d\beta \int_0^{2\pi} d\alpha p(\alpha, \beta, \gamma) \xi_{yy} = \frac{1}{3} (\xi_{x'} + \xi_{y'} + \xi_{z'}) \quad (\text{B5b})$$

$$\langle \xi_{zz} \rangle = \int_0^{2\pi} d\gamma \int_0^\pi d\beta \int_0^{2\pi} d\alpha p(\alpha, \beta, \gamma) \xi_{zz} = \frac{1}{3} (\xi_{x'} + \xi_{y'} + \xi_{z'}) \quad (\text{B5c})$$

$$\langle \xi_{xy} \rangle = \langle \xi_{yx} \rangle = \int_0^{2\pi} d\gamma \int_0^\pi d\beta \int_0^{2\pi} d\alpha p(\alpha, \beta, \gamma) \xi_{yx} = 0 \quad (\text{B5d})$$

$$\langle \xi_{xz} \rangle = \langle \xi_{zx} \rangle = \int_0^{2\pi} d\gamma \int_0^\pi d\beta \int_0^{2\pi} d\alpha p(\alpha, \beta, \gamma) \xi_{zx} = 0 \quad (\text{B5e})$$

$$\langle \xi_{yz} \rangle = \langle \xi_{zy} \rangle = \int_0^{2\pi} d\gamma \int_0^\pi d\beta \int_0^{2\pi} d\alpha p(\alpha, \beta, \gamma) \xi_{zy} = 0 \quad (\text{B5f})$$

For generality, subscript  $i$  for the scatterer species  $i$  and  $b$  for the background are not included in the notation of  $\xi_{j'}$  ( $j' = x', y', z'$ ) which can take on the value of  $\xi_{ij'}$  for scatterer species  $i = 1, 2, 3, \dots, N$  or  $\xi_{bj'}$  for the background. The above results are used to obtain (9). When  $\xi$  is replaced by  $S$ , (12) is obtained.

### C. Coefficients in Variances

Polarimetric scattering coefficients derived in this paper involve the term  $\Delta_{tnjklm}$  which are integrals over the Eulerian angles of the probability density function of the random orientation and the variances in the global coordinates.  $\Delta_{tnjklm}$  is considered a variance averaged over the orientation and defined by

$$\Delta_{tnjklm} = \sum_{u,v}^{x,y,z} \int_0^{2\pi} d\gamma \int_0^\pi d\beta \int_0^{2\pi} d\alpha p_n(\alpha, \beta, \gamma) \delta_{tnuv} a_{ujk} a_{vlm}$$

There are six subscripts associated with coefficient  $a$ 's in the above equation. Each subscript can be  $x, y, \text{ or } z$ ; therefore, there are  $3^6 = 729$  terms in total. After being integrated,

540 terms become zero and the remaining non-zero terms are presented in this appendix.

Coefficient  $a$ 's, given in appendix B, come from the rotation operation on the tensors. For

instance, consider the following integration of the product of the orientation probability

and  $a_{xxx}a_{xxx}$

$$\begin{aligned}
& \int_0^{2\pi} d\gamma \int_0^\pi d\beta \int_0^{2\pi} d\alpha p_n(\alpha, \beta, \gamma) a_{xxx}a_{xxx} \\
&= \int_0^{2\pi} d\gamma \int_0^\pi \beta \int_0^{2\pi} d\alpha \frac{\sin \beta}{8\pi^2} \\
& \left[ \cos^4 \gamma \cos^4 \beta \cos^4 \alpha + \sin^4 \gamma \sin^4 \alpha \right. \\
& + 4 \sin^4 \gamma \cos^2 \gamma \cos^2 \beta \sin^2 \alpha \cos^2 \alpha \\
& + 2 \sin^2 \gamma \cos^2 \gamma \cos^2 \beta \sin^2 \alpha \cos^2 \alpha \\
& - 4 \sin \gamma \cos^3 \gamma \cos^3 \beta \sin \alpha \cos^3 \alpha \\
& \left. - 4 \sin^3 \gamma \cos \gamma \cos \beta \sin^3 \alpha \cos \alpha \right] = \frac{1}{5}
\end{aligned}$$

The results of the integrations show that many combinations of  $a$ 's have one of the values:  $1/5$ ,  $2/15$ ,  $1/15$ , or  $-1/30$ . Actually, the results can be written in compact forms due to the symmetry in the combinations of the subscripts. By defining the averaging operator  $L$  as

$$L = \int_0^{2\pi} d\gamma \int_0^\pi d\beta \int_0^{2\pi} d\alpha p_n(\alpha, \beta, \gamma) \quad (\text{C1})$$

the non-zero terms can simply be expressed as

$$La_{uvv}a_{uvv} = 1/5 \quad (\text{C2a})$$

$$La_{rvv}a_{sww} = 2/15 \quad (\text{C2b})$$

$$La_{uvv}a_{uww} = La_{uvv}a_{uvv} = La_{uvv}a_{uuv} = La_{uww}a_{vww} = 1/15 \quad (\text{C2c})$$

$$La_{rvv}a_{svv} = La_{rvv}a_{sww} = -1/30 \quad (\text{C2d})$$

where subscript  $r$ ,  $s$ ,  $u$ ,  $v$ , or  $w$  can be  $x$ ,  $y$ , or  $z$ . Followed are some examples

$$\int_0^{2\pi} d\gamma \int_0^\pi d\beta \int_0^{2\pi} d\alpha p(\alpha, \beta, \gamma) a_{xxx}a_{xxx} = 1/5 \quad (\text{C3a})$$

$$\int_0^{2\pi} d\gamma \int_0^\pi d\beta \int_0^{2\pi} d\alpha p(\alpha, \beta, \gamma) a_{xxx}a_{yyy} = 2/15 \quad (\text{C3b})$$

$$\int_0^{2\pi} d\gamma \int_0^\pi d\beta \int_0^{2\pi} d\alpha p(\alpha, \beta, \gamma) a_{xxx}a_{zxx} = 1/15 \quad (\text{C3c})$$

$$\int_0^{2\pi} d\gamma \int_0^\pi d\beta \int_0^{2\pi} d\alpha p(\alpha, \beta, \gamma) a_{yxy}a_{xxy} = -1/30 \quad (\text{C3d})$$

*Acknowledgments.* The research described in this paper was carried out by the Jet Propulsion Laboratory, California Institute of Technology, and was sponsored by the Office of Naval Research and the National Aeronautics and Space Administration; and by the Massachusetts Institute of Technology, under contracts N00014-89-J-1107 and N00014-92-J-4098 with the Office of Naval Research.

## REFERENCES

- Ding, K. H., and L. Tsang, Effective propagation constants in media with densely distributed dielectric particles of multiples sizes and permittivities, *Progress in Electromagnetics Research*, vol. 1, chap. 3, ed. by J. A. Kong, pp. 241-295, Elsevier, New York, 1989.
- Lang, R. H., R. Landry, Ö Kiliç, N. Chauhan, N. Khadr, and D. Leckie, Effect of species structure and dielectric constant on C-band forest backscatter, *Proceeding of the IGARSS'99 Symposium*, Tokyo, Japan, 583-586, 1993.
- Maykut, G. A., Large-scale heat exchange and ice production in the central Arctic, *J.*

*Geophys. Res.* 87(C10), 7971-7984, 1982.

Nghiem, S. V., M. Borgeaud, J. A. Kong, and R. T. Shin, Polarimetric remote sensing of geophysical media with layer random medium model, *Progress in Electromagnetics Research, vol. 3: Polarimetric Remote Sensing*, chap. 1, ed. by J. A. Kong, pp. 1-73, Elsevier, New York, 1990.

Nghiem, S. V., T. Le Toan, J. A. Kong, H. C. Han, and M. Borgeaud, Layer model with random spheroidal scatterers for remote sensing of vegetation canopy, *J. Electromagn. Waves Appl.*, 7(1), 49-76, 1993a.

Nghiem, S. V., R. Kwok, J. A. Kong, and R. T. Shin, A model with ellipsoidal scatterers for polarimetric remote sensing of anisotropic layered media, *Radio Sci.*, 28(5), 687-703, 1993b.

Nghiem, S. V., R. Kwok, S. H. Yueh, J. A. Kong, M. A. Tassoudji, C. C. Hsu, A. J. Gow, and D. K. Perovich, Polarimetric backscattering signatures from thin saline ice under controlled laboratory conditions, *Int. Geosci. and Rem. Sens. Symp.*, Pasadena, California, August 8-12, 1994.

Perovich, D. K., and J. A. Richter-Menge, Surface characteristics of lead ice, *J. Geophys. Res.*, 99(C8), 16341-16350, 1994.

Sihvola, A. H., and J. A. Kong, Effective permittivity of dielectric mixtures, *IEEE Trans. Geosci. Remote Sens.*, 26(4), 420-429, 1988.

Stogryn, A., An analysis of the tensor dielectric constant of sea ice at microwave frequencies, *IEEE Trans. Geosci. Remote Sens.*, GE-25(2), 147-158, 1987.

Thomas, R. H., R. A. Bindschadler, R. L. Cameron, F. D. Carsey, B. Holt, T. J. Hughes, C. M. W. Swithinbank, I. M. Willans, and H. J. Zwally, Satellite remote sensing for

- ice sheet research, *NASA Tech. Memo. 86233*, 1985.
- Tinga, W. R., W. A. G. Voss, and D. F. Blossey, Generalized approach to multiphase dielectric mixture theory, *J. Applied Phys.*, *44*(9), 3897-3902, 1973.
- Tjuatja, S., A. K. Fung, and J. Bredow, A scattering model for snow-covered sea ice, *IEEE Trans. Geosci. Remote Sens.*, *30*(4), 804-810, 1992.
- Tsang, L., and J. A. Kong, Scattering of electromagnetic waves from random media with strong permittivity fluctuations, *Radio Sci.*, *16*(3), 303-320, 1981a.
- Tsang, L., and J. A. Kong, Application of strong fluctuation random medium theory to scattering from vegetation-like half space, *IEEE Trans. Geosci. Remote Sens.*, *19*(1), 62-69, 1981b.
- Tsang, L., J. A. Kong, and R. W. Newton, Application of strong fluctuation random medium theory to scattering of electromagnetic waves from a half-space of dielectric mixture, *IEEE Trans. Antennas Propagat.*, *30*(2), 292-302, 1982.
- Tsang, L., K. H. Ding, and B. Wen, Polarimetric signatures of random discrete scatterers based on radiative transfer theory, *Progress in Electromagnetics Research*, vol. 3: *Polarimetric Remote Sensing*, chap. 2, ed. by J. A. Kong, pp. 75-142, Elsevier, New York, 1990.
- Wait, J. R., Effective electrical properties of heterogeneous earth models, *Radio Sci.*, *18*(1), 19-24, 1983.
- Yueh, H. A., R. T. Shin, and J. A. Kong, Scattering from randomly oriented scatterers with strong permittivity fluctuations, *J. Electromagn. Waves Appl.*, *4*(10), 983-1004, 1990.

## Figure Captions

- Figure 1.** Inhomogeneous media with multiple species of scatterers.
- Figure 2.** Parameters to study effects of scatterer shapes.
- Figure 3.** Copolarized backscattering coefficients  $H = \sigma_{hh}$  and  $V = \sigma_{vv}$  for different scatterer shapes.
- Figure 4.** Cross-polarized backscattering coefficients for different scatterer shapes.
- Figure 5.** Magnitudes of correlation coefficient  $\rho$  for different scatterer shapes.
- Figure 6.** Parameters to study effects of multiple species.
- Figure 7.** Backscattering coefficients for different mixtures of multiple species. For each mixture, the top curve is for  $\sigma_{hh}$ , middle for  $\sigma_{vv}$ , and bottom for  $\sigma_{hv}$ .
- Figure 8.** Magnitudes of correlation coefficient  $\rho$  for different mixtures of multiple species.
- Figure 9.** Intensity ratio  $e = \sigma_{hv}/\sigma_{hh}$  for different mixtures of multiple species.
- Figure 10.** Parameters of a half-space multi-species model for dry and wet snowpack.
- Figure 11.** Backscattering coefficient  $\sigma_{vv}$  as a function of grain size for various moisture contents.
- Figure 12.** Parameters of a layered multi-species model for frost-covered saline ice.
- Figure 13.** Polarimetric scattering results for bare and frost-covered saline ice: square, circle, and X are for measured data from CRRELEX93 for bare saline ice; continuous curves without symbol S are model results for bare saline ice; and continuous curves with

symbol S are model results for frost-covered saline ice.

**Figure 14.** Normalized copolarized polarimetric signatures of (a) bare and (b) frost-covered saline ice.

**Figure A.1.** Eulerian angles : (a)  $\alpha$  is the rotation angle about  $z'$  axis, (b)  $\beta$  is the rotation angle about  $y_1$  axis, and (c)  $\gamma$  is the rotation angle about  $z_2$  axis.

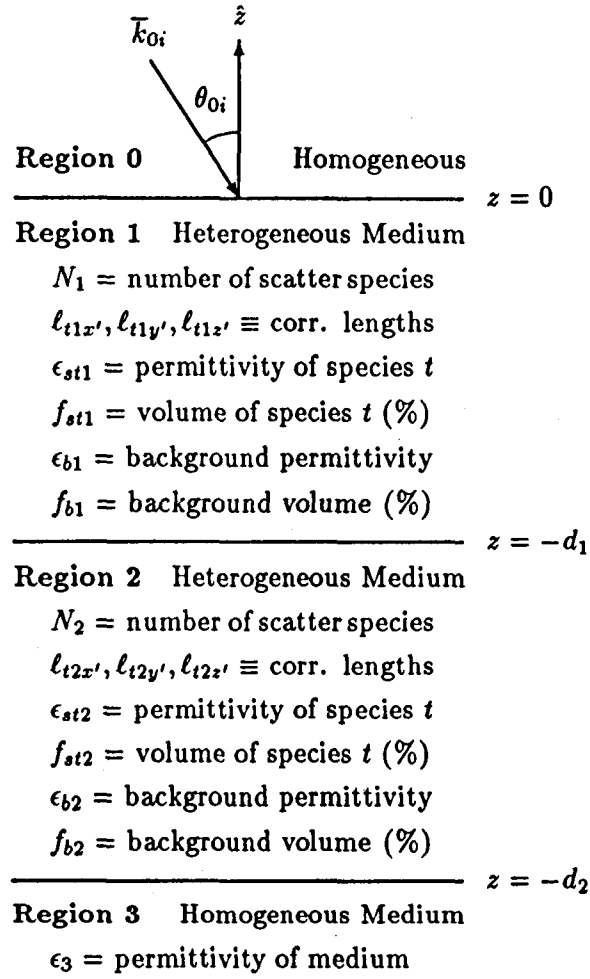


Figure 1

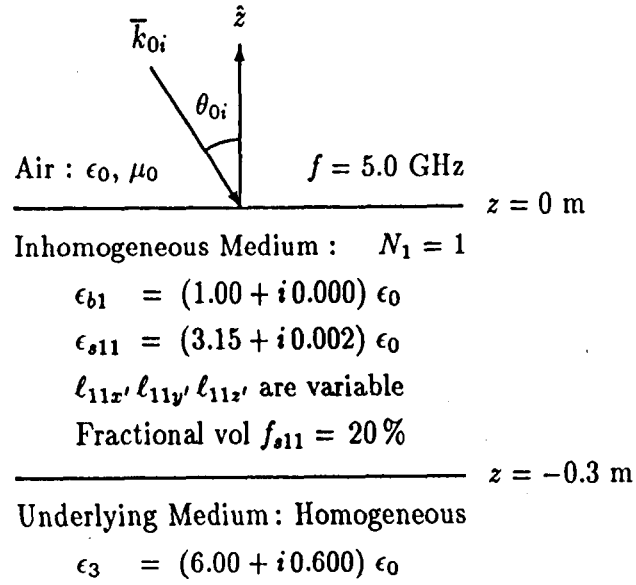


Figure 2

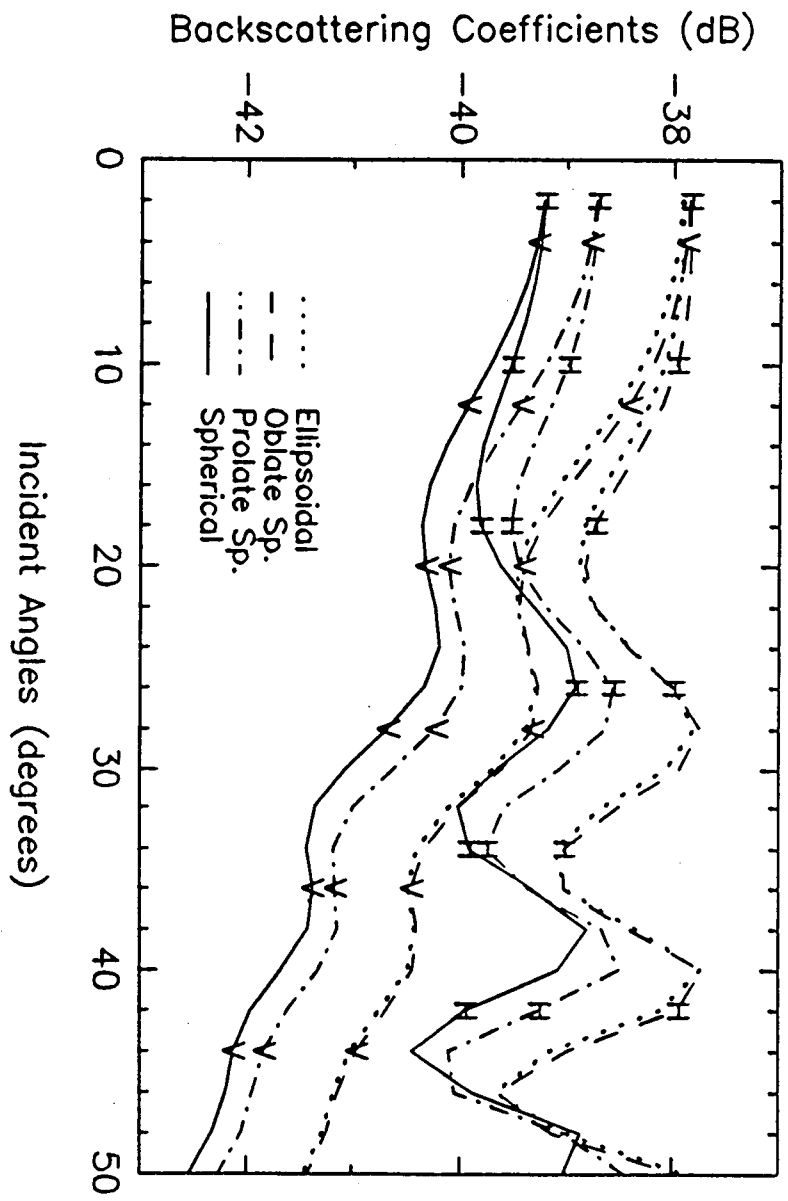


FIG. 3

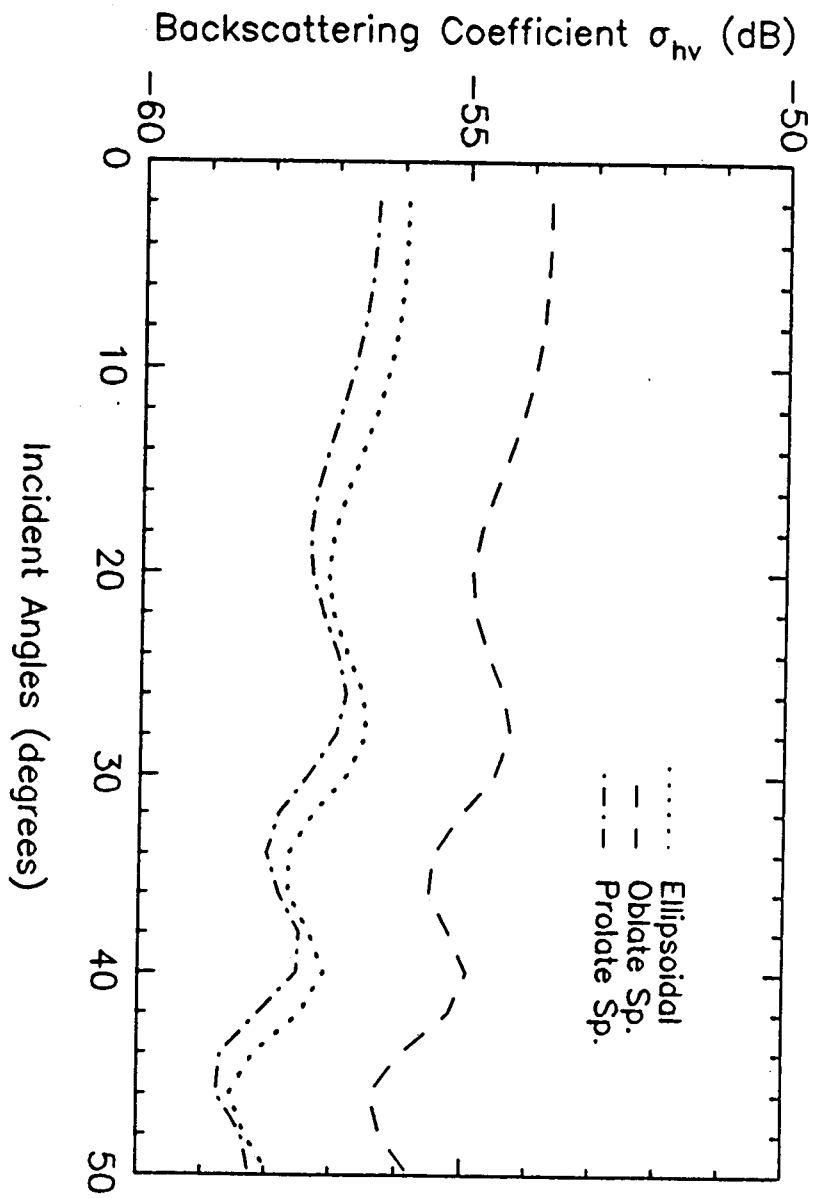


FIG. 4

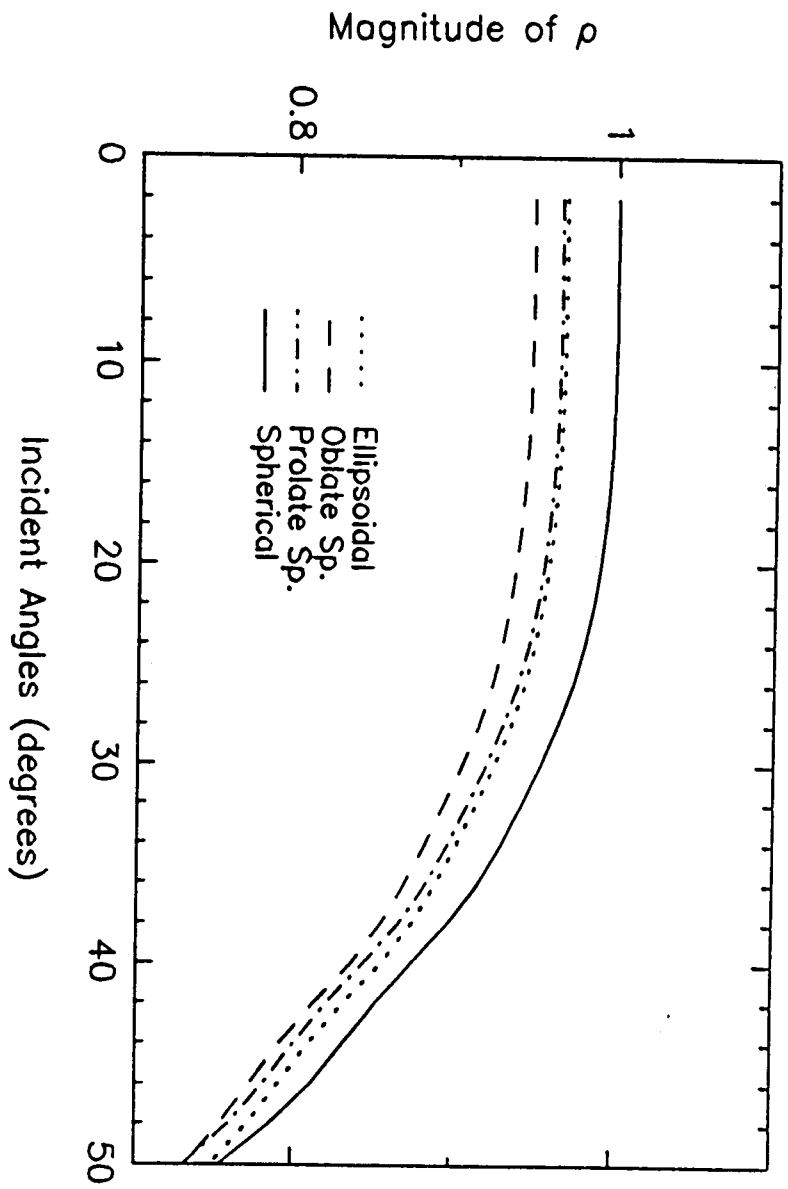


FIG . 5

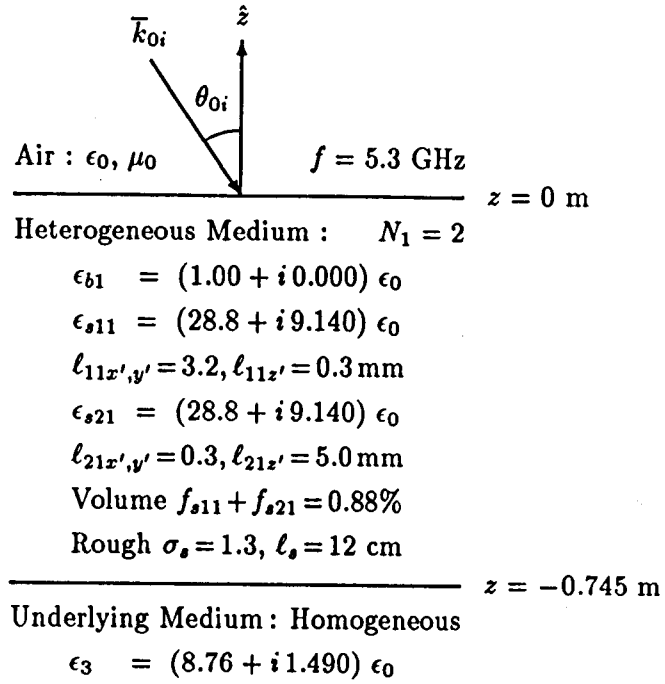
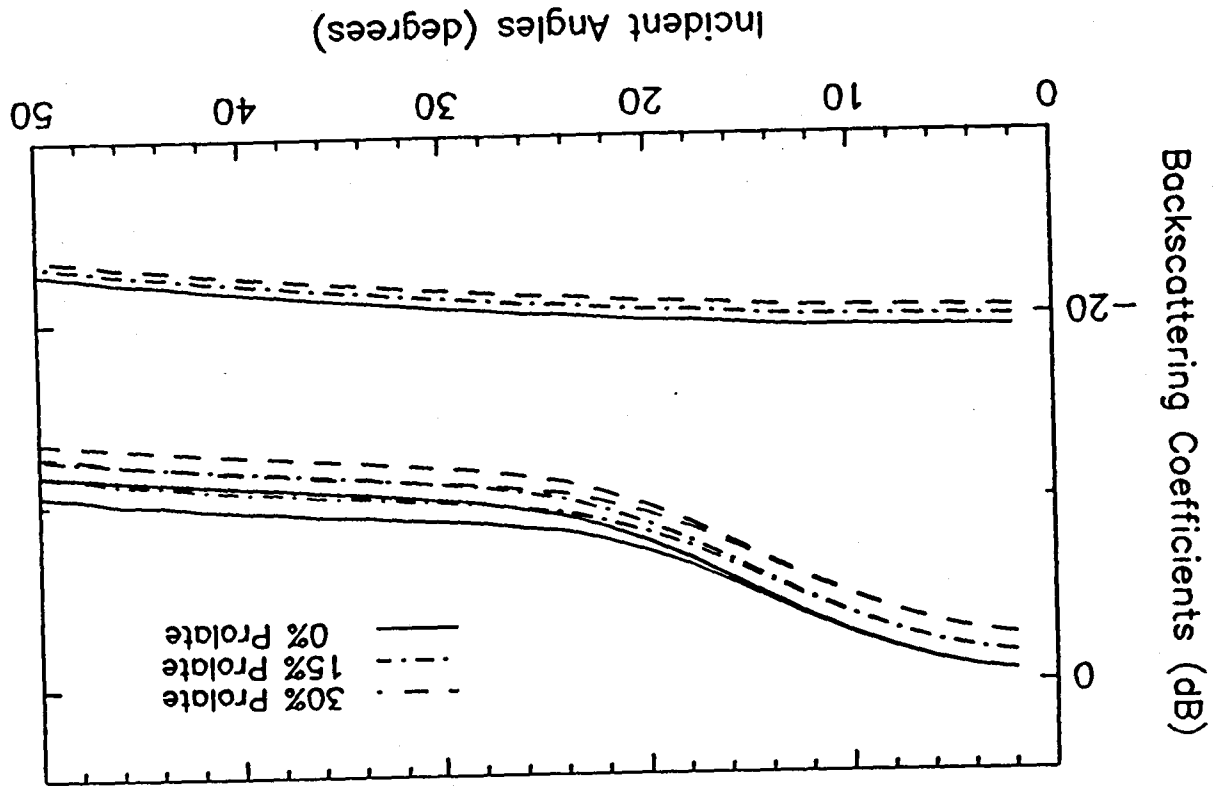


Figure 6

FIG. 7



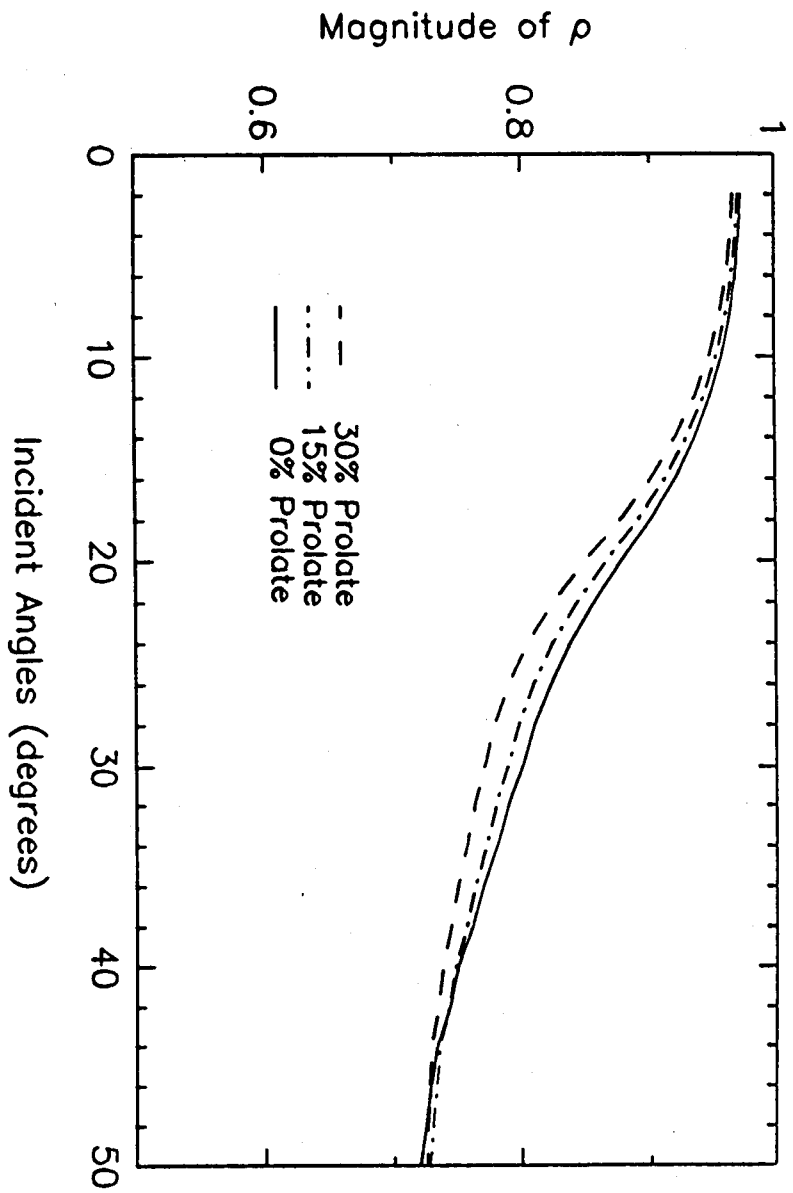


FIG. 8

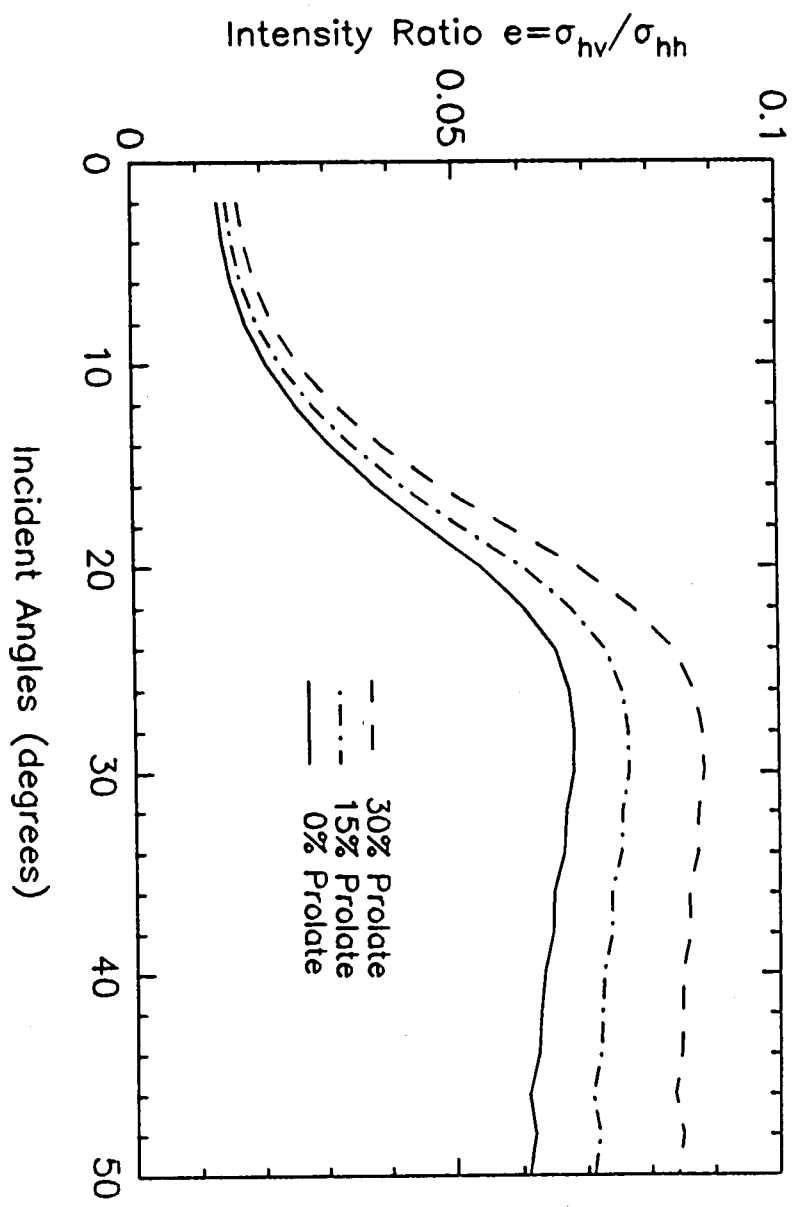


FIG. 9

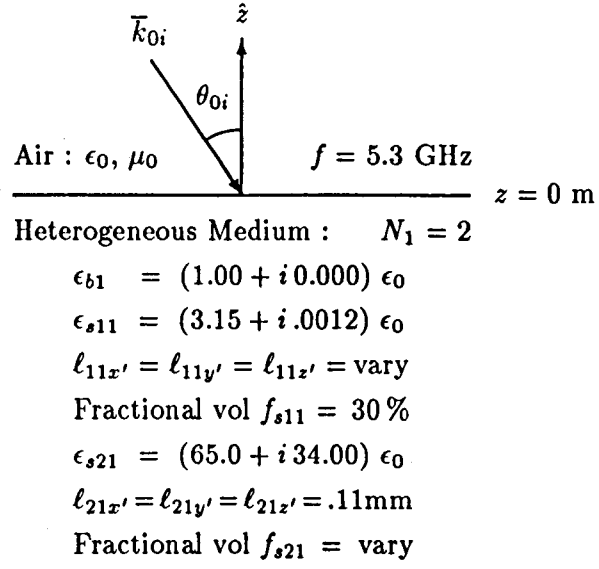


Figure 10

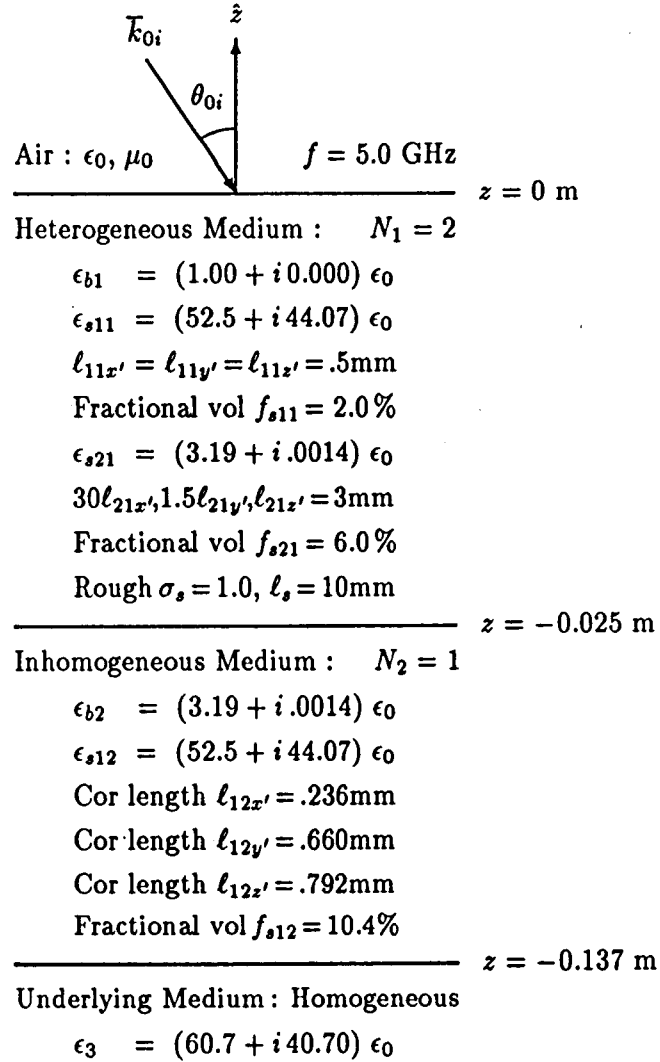
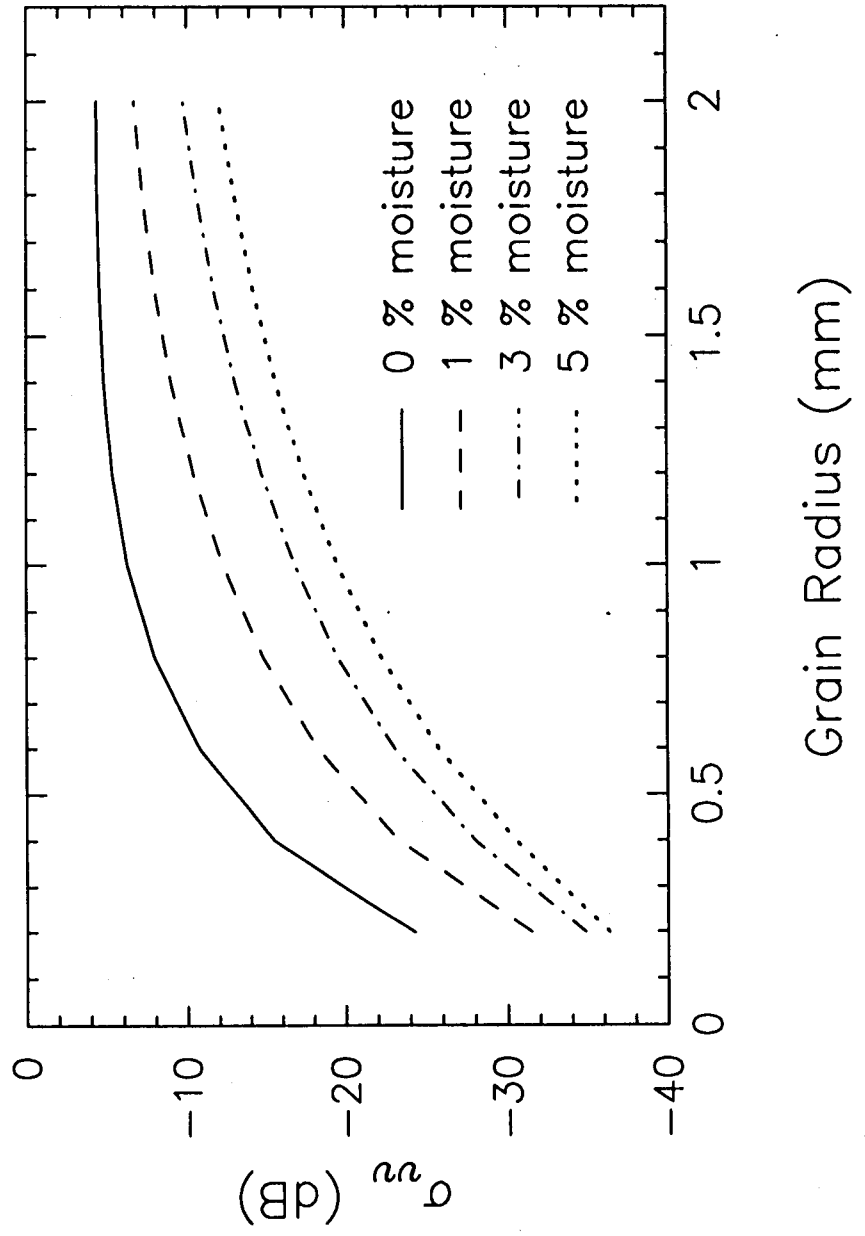
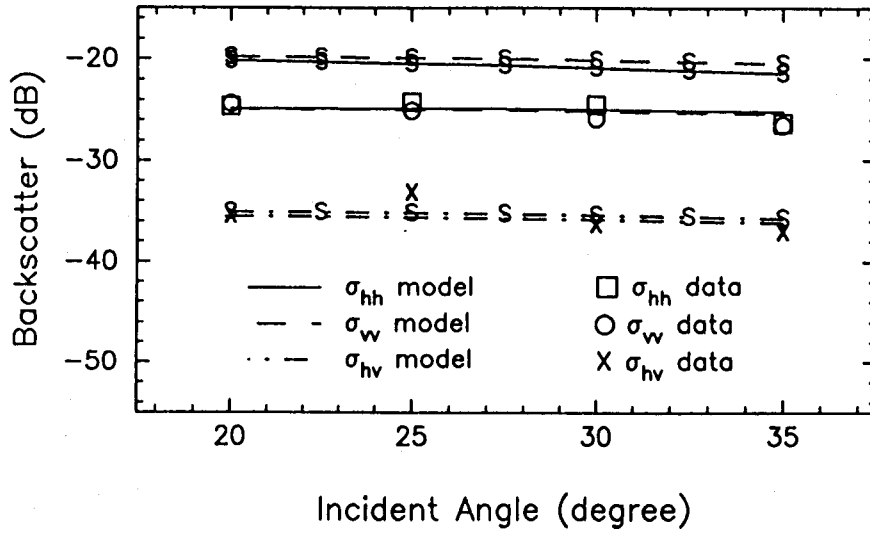


Figure 12

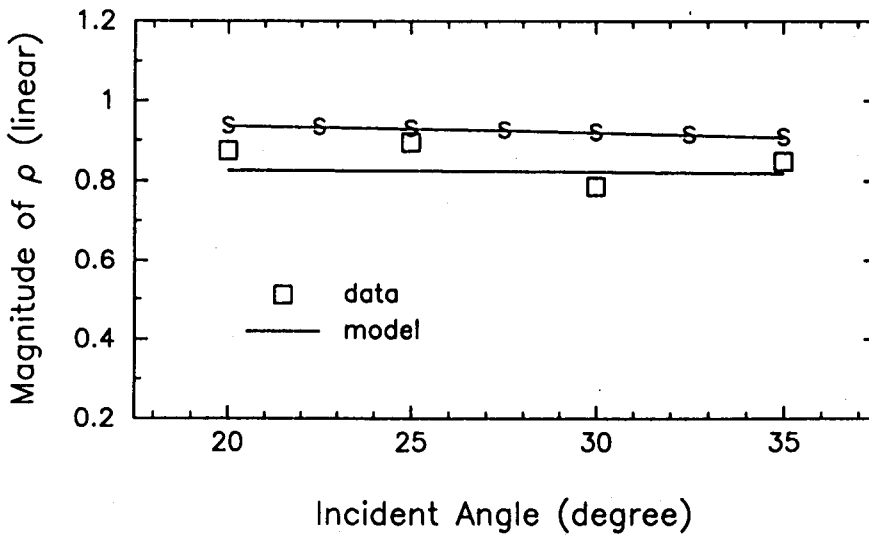
FIG. 11



(a) Backscatter (Thickness = 11.2 cm)



(b) Magnitude of Correlation Coefficient  $\rho$



(c) Phase of Correlation Coefficient  $\rho$

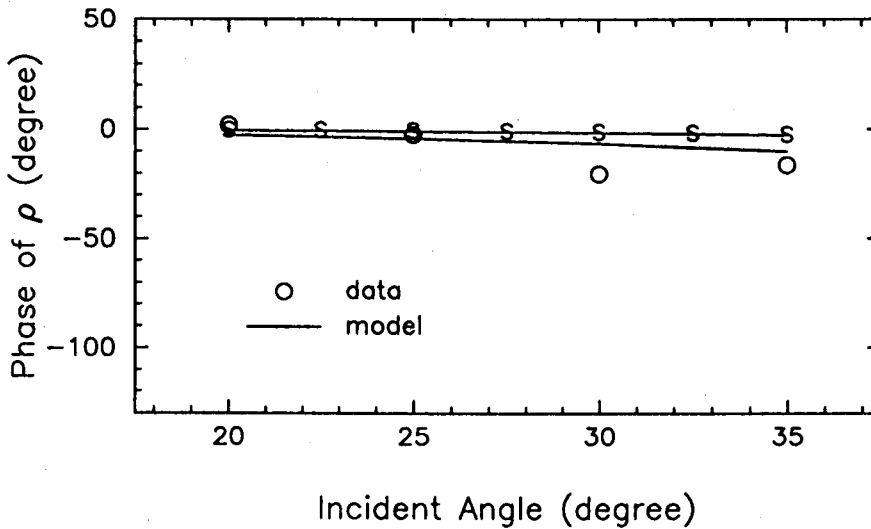


FIG. 13

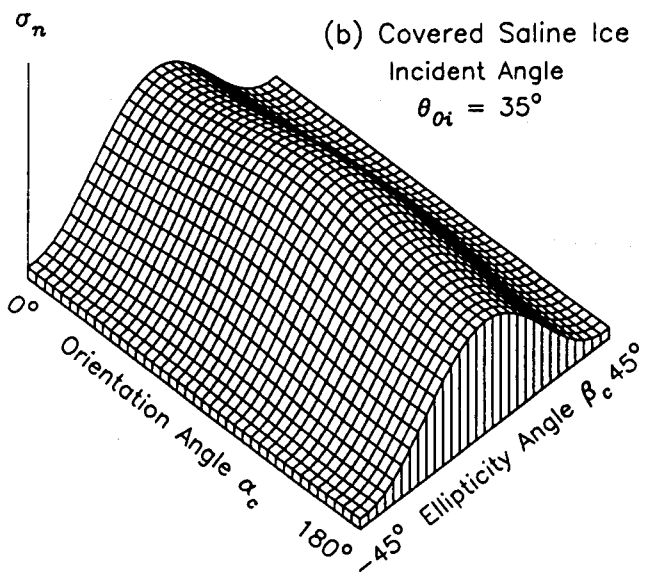
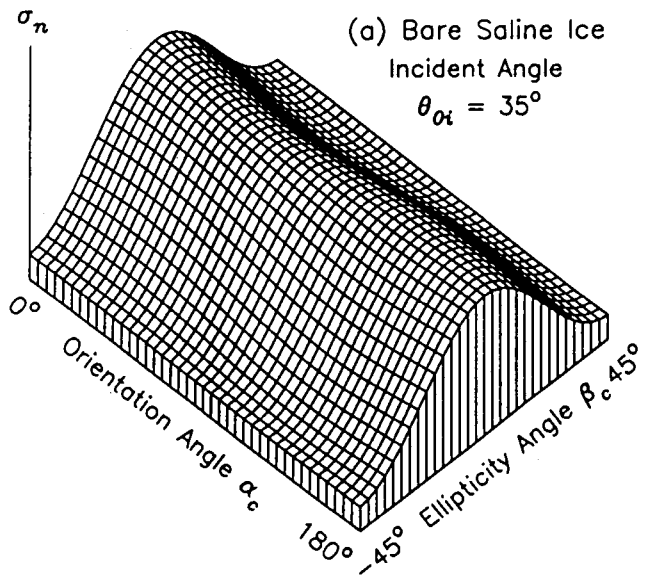
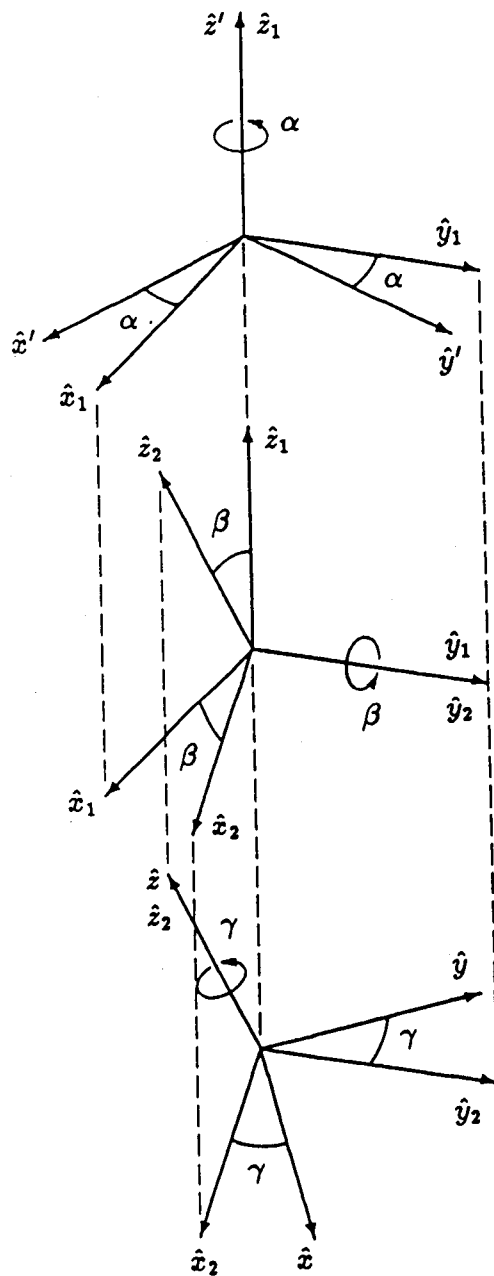


FIG . 14



(a)

$$\bar{\bar{T}}_{\alpha} = \begin{bmatrix} \cos \alpha & \sin \alpha & 0 \\ -\sin \alpha & \cos \alpha & 0 \\ 0 & 0 & 1 \end{bmatrix}$$

(b)

$$\bar{\bar{T}}_{\beta} = \begin{bmatrix} \cos \beta & 0 & -\sin \beta \\ 0 & 1 & 0 \\ \sin \beta & 0 & \cos \beta \end{bmatrix}$$

(c)

$$\bar{\bar{T}}_{\gamma} = \begin{bmatrix} \cos \gamma & \sin \gamma & 0 \\ -\sin \gamma & \cos \gamma & 0 \\ 0 & 0 & 1 \end{bmatrix}$$

Figure A1